

REPORT DOCUMENTATION PAGE			Form Approved OMB NO. 0704-0188		
<p>The public reporting burden for this collection of information is estimated to average 1 hour per response, including the time for reviewing instructions, searching existing data sources, gathering and maintaining the data needed, and completing and reviewing the collection of information. Send comments regarding this burden estimate or any other aspect of this collection of information, including suggestions for reducing this burden, to Washington Headquarters Services, Directorate for Information Operations and Reports, 1215 Jefferson Davis Highway, Suite 1204, Arlington VA, 22202-4302. Respondents should be aware that notwithstanding any other provision of law, no person shall be subject to any penalty for failing to comply with a collection of information if it does not display a currently valid OMB control number.</p> <p>PLEASE DO NOT RETURN YOUR FORM TO THE ABOVE ADDRESS.</p>					
1. REPORT DATE (DD-MM-YYYY) 27-10-2014		2. REPORT TYPE Final Report		3. DATES COVERED (From - To) 3-May-2011 - 2-May-2014	
4. TITLE AND SUBTITLE Final Report: Libration Point Orbit Utilization for Tactical Advantage in Communications, Surveillance, and Risk Mitigation			5a. CONTRACT NUMBER W911NF-11-1-0195		
			5b. GRANT NUMBER		
			5c. PROGRAM ELEMENT NUMBER 206022		
6. AUTHORS Dr. Eric Butcher			5d. PROJECT NUMBER		
			5e. TASK NUMBER		
			5f. WORK UNIT NUMBER		
7. PERFORMING ORGANIZATION NAMES AND ADDRESSES New Mexico State University Box 30002, MSC OGC Anderson Hall E1200, Espina and Stewart Streets Las Cruces, NM 88003 -8002			8. PERFORMING ORGANIZATION REPORT NUMBER		
9. SPONSORING/MONITORING AGENCY NAME(S) AND ADDRESS (ES) U.S. Army Research Office P.O. Box 12211 Research Triangle Park, NC 27709-2211			10. SPONSOR/MONITOR'S ACRONYM(S) ARO		
			11. SPONSOR/MONITOR'S REPORT NUMBER(S) 59022-NS-REP.14		
12. DISTRIBUTION AVAILABILITY STATEMENT Approved for Public Release; Distribution Unlimited					
13. SUPPLEMENTARY NOTES The views, opinions and/or findings contained in this report are those of the author(s) and should not be construed as an official Department of the Army position, policy or decision, unless so designated by other documentation.					
14. ABSTRACT Final Report					
15. SUBJECT TERMS					
16. SECURITY CLASSIFICATION OF:			17. LIMITATION OF ABSTRACT UU	15. NUMBER OF PAGES	19a. NAME OF RESPONSIBLE PERSON Eric Butcher
a. REPORT UU	b. ABSTRACT UU	c. THIS PAGE UU			19b. TELEPHONE NUMBER 575-646-6179

Report Title

Final Report: Libration Point Orbit Utilization for Tactical Advantage in Communications, Surveillance, and Risk Mitigation

ABSTRACT

Final Report

Enter List of papers submitted or published that acknowledge ARO support from the start of the project to the date of this printing. List the papers, including journal references, in the following categories:

(a) Papers published in peer-reviewed journals (N/A for none)

Received

Paper

08/29/2013 4.00 Kathryn Davis, George Born, Eric Butcher. Transfers to Earth–Moon L3 halo orbits, Acta Astronautica, (07 2013): 116. doi: 10.1016/j.actaastro.2013.03.004

TOTAL: 1

Number of Papers published in peer-reviewed journals:

(b) Papers published in non-peer-reviewed journals (N/A for none)

Received

Paper

TOTAL:

Number of Papers published in non peer-reviewed journals:

(c) Presentations

Number of Presentations: 0.00

Non Peer-Reviewed Conference Proceeding publications (other than abstracts):

Received

Paper

08/29/2013 10.00 Nathan Parrish, Jeffrey Parker, Ben Bradley. GEO Observability from Earth-Moon Libration Point Orbits, 2013 AAS Spaceflight Mechanics Conference. 10-FEB-13, . : ,

08/29/2013 7.00 Daero Lee, Eric Butcher, Amit Sanyal. Optimal Mixed Impulsive/Continuous Thrust Trajectories to the Interior Earth-Moon L1 Lagrange Point, 2013 AAS Spaceflight Mechanics Conference. 10-FEB-13, . : ,

TOTAL: 2

Number of Non Peer-Reviewed Conference Proceeding publications (other than abstracts):

Peer-Reviewed Conference Proceeding publications (other than abstracts):

Received

Paper

08/24/2012 1.00 George Born, Masoud Deilami, Annie Larsen, Kathryn Davis, Eric Butcher. Transfers to Earth-Moon L3 Halo Orbits, AIAA/AAS Astrodynamics Specialist Conference. 12-AUG-12, . : ,

08/24/2012 2.00 William Anthony, Thomas Critz, Morad Nazari, Masoud Deilami, Annie Larsen, Eric Butcher, George Born, Jay McMahon. Optimal Transfers with Guidance to the Earth-Moon L1 and L3 Libration Points using Invariant Manifolds: A Preliminary Study, AIAA/AAS Astrodynamics Specialist Conference. 12-AUG-12, . : ,

08/29/2013 9.00 Kathryn Davis, Nathan Parrish, George Born, Eric Butcher. Earth Coverage from Earth-Moon Libration Point Orbits, 2013 Astrodynamics Specialist Conference. 11-AUG-13, . : ,

08/29/2013 6.00 William Anthony, Annie Larsen, Eric Butcher, Jeffrey Parker. Impulsive Guidance for Optimal Manifold-Based Transfers to Earth-Moon L1 Halo Orbits, 2013 Astrodynamics Specialist Conference. 11-AUG-13, . : ,

08/29/2013 5.00 William Anthony, Annie Larsen, Eric Butcher. Optimal Impulsive Manifold-Based Transfers with Guidance to L1 Halo Orbits, 2013 AAS Spaceflight Mechanics Conference. 10-FEB-13, . : ,

TOTAL: 5

Number of Peer-Reviewed Conference Proceeding publications (other than abstracts):

(d) Manuscripts

<u>Received</u>		<u>Paper</u>
08/31/2012	3.00	Nathan Parrish, Jeffrey Parker, Benjamin Bradley, George Born. GEO Observability from Earth-Moon Libration Point Orbits, (09 2012)
TOTAL:		1

Number of Manuscripts:

Books

<u>Received</u>	<u>Book</u>
TOTAL:	

<u>Received</u>	<u>Book Chapter</u>
TOTAL:	

Patents Submitted

Patents Awarded

Awards

Graduate Students

<u>NAME</u>	<u>PERCENT SUPPORTED</u>
FTE Equivalent:	
Total Number:	

Names of Post Doctorates

<u>NAME</u>	<u>PERCENT SUPPORTED</u>
FTE Equivalent:	
Total Number:	

Names of Faculty Supported

<u>NAME</u>	<u>PERCENT SUPPORTED</u>
FTE Equivalent:	
Total Number:	

Names of Under Graduate students supported

<u>NAME</u>	<u>PERCENT SUPPORTED</u>
FTE Equivalent:	
Total Number:	

Student Metrics

This section only applies to graduating undergraduates supported by this agreement in this reporting period

The number of undergraduates funded by this agreement who graduated during this period: 0.00

The number of undergraduates funded by this agreement who graduated during this period with a degree in science, mathematics, engineering, or technology fields:..... 0.00

The number of undergraduates funded by your agreement who graduated during this period and will continue to pursue a graduate or Ph.D. degree in science, mathematics, engineering, or technology fields:..... 0.00

Number of graduating undergraduates who achieved a 3.5 GPA to 4.0 (4.0 max scale):..... 0.00

Number of graduating undergraduates funded by a DoD funded Center of Excellence grant for Education, Research and Engineering:..... 0.00

The number of undergraduates funded by your agreement who graduated during this period and intend to work for the Department of Defense 0.00

The number of undergraduates funded by your agreement who graduated during this period and will receive scholarships or fellowships for further studies in science, mathematics, engineering or technology fields: 0.00

Names of Personnel receiving masters degrees

<u>NAME</u>
Total Number:

Names of personnel receiving PhDs

<u>NAME</u>
Total Number:

Names of other research staff

<u>NAME</u>	<u>PERCENT SUPPORTED</u>
FTE Equivalent:	
Total Number:	

Sub Contractors (DD882)

Inventions (DD882)

Scientific Progress

Technology Transfer

Libration Point Orbit Utilization for Tactical Advantage in Communications, Surveillance, and Risk
Mitigation

US Army Award W911NF-11-1-0195

Eric Butcher, Principal Investigator

New Mexico State University

Final Report

Contents

Project Summary.....	3
Technical Background	
A. Problem Formulation.....	3
B. Lagrange Points.....	3
C. Periodic Orbits about Lagrange Points.....	4
D. Stability of Libration Points and Halo Orbits.....	4
E. Invariant Manifolds.....	5
F. Pseudo-Manifolds.....	5
G. Earth Coverage and GEO Surveillance from Libration Point Orbits.....	6
Summary of the Most Important Results	
A. Optimal Transfers to L_1 , L_3 , and L_1 Halo Orbits.....	6
B. Analysis of Thrust Dispersion Effects.....	7
C. LQR-Based Continuous Thrust Guidance.....	8
D. Impulsive Guidance.....	8
E. Optimal Mixed Impulsive/Continuous Thrust Transfers to L_1 Liapunov Orbits.....	9
F. Efficient Transfers to L_3 Halo Orbits.....	9
G. GEO Observability Analysis from Libration Point Orbits.....	11
H. Earth Observability Analysis from Libration Point Orbits.....	13
Bibliography.....	14
List of Figures.....	17

Project Summary

This project focuses on the benefits and challenges associated with the utilization of Earth-Moon (lunar) libration point orbits (LPOs) for communications with and surveillance from military satellites. DoD-relevant topical areas include Space Situational Awareness and Operationally Responsive Space capabilities with emphasis on Space-Based Space Surveillance (SBSS), orbital camouflage, and reducing risks of both purposeful interference and collisions with space debris that are associated with space assets in low Earth (LEO) or geosynchronous (GEO) orbit. In the first year of the project efforts concentrated on 1) finding fuel-optimal invariant manifold-based transfers via impulsive maneuvers to the lunar L_1 and L_3 Lagrange points, 2) studying Earth and GEO observability from single and multiple LPOs, and 3) analysis of thrust dispersion errors at manifold injection and the development of guidance laws to mitigate their effects. In the second year efforts concentrated on 1) finding fuel-optimal transfers via impulsive maneuvers to a selection of halo orbits about the lunar L_1 and L_3 LPOs, 2) finding fuel-optimal transfers to a Liapunov orbit about the lunar L_1 point using mixed impulsive and continuous thrust, 3) studying Earth and GEO observability from single LPO about the L_1 and L_3 points and a constellation of spacecraft in multiple L_1 and L_3 LPOs, and 4) the development of continuous (LQR-based) and impulsive guidance laws to mitigate the effects of thrust errors for the optimal impulsive manifold-based transfers to the L_1 LPO. In the third year efforts have concentrated on 1) obtaining improved impulsive transfers from Earth to a halo orbit about the lunar L_3 point, 2) obtaining statistical fuel budgets for impulsive guidance for use in fuel-optimal transfers to lunar L_1 LPOs, 3) obtaining low-cost periodic-gain feedback control laws for station keeping about lunar L_1 LPOs and comparing their performance with more traditional control schemes. In total ten conference papers [1-10] and one published journal paper [11] resulted from this investigation, as well as three more currently in review or preparation [12-14]. In addition, portions of the results from this project were presented in two talks [15-16] by the PI, one of which was given at the Air Force Research Laboratories, Kirtland AFB, Albuquerque. The following subsections outline the main contributions.

Technical Background

A. Problem Formulation

The Circular Restricted Three-Body Problem (CR3BP) models the motion of a particle of negligible mass under the influence of two larger bodies, or primaries (Figure 1). The larger of the bodies is termed the primary and the smaller is termed the secondary. The primaries rotate in circular orbits about the system barycenter. Additionally, the reference frame rotates about the barycenter at the same rotation rate as the two primaries. The x-axis extends from the origin through the secondary, the z-axis extends in the direction of the angular momentum of the system, and the y-axis completes the right-hand coordinate frame. The reader is directed to Szebehely [17] for a derivation of the equations of motion. The Jacobi Constant, C , is the only integral of motion which emerges in the rotating system.

B. Lagrange Points

The CR3BP has five equilibrium points with coordinates (x_e, y_e, z_e) called Lagrange or libration points and denoted by L_1 - L_5 . These points can be found by setting the derivatives in the CR3BP equations equal to

zero. Using this procedure, one can see that for three of them, called the collinear libration points L_1 - L_3 , the y_e and z_e components are zero. For the Earth-Moon system with gravitational constant $\mu=0.01215$, the libration points are located from the barycenter with the following dimensionless coordinates (for distances in km multiply by the average Earth-Moon distance 384,400 km): L_1 : $(x_e, y_e, z_e)=(0.8369, 0, 0)$, L_2 : $(1.156, 0, 0)$, and L_3 : $(-1.005, 0, 0)$. Two other equilibrium points L_4 and L_5 (called triangular points) are located at $(x_e, y_e, z_e)=(0.48785, \pm 0.86603, 0)$. All five Lagrange points of Earth-Moon system have been shown in Figure 1.

C. Periodic Orbits about Lagrange Points

Families of periodic and quasi-periodic orbits which exist about the libration points have been studied extensively by many researchers [18]. The quasi-periodic orbits around libration points are called Lissajous orbits which wind around a torus but never repeat [19]. Halo orbits are a special case of Lissajous orbits where the in-plane and out-of-plane frequencies are equal thus producing periodic motion, and were discovered by Farquhar [24]. Large amplitude lunar halo orbits appear to form a halo about the Moon when viewed from the Earth [20, 25]. Halo orbits are three-dimensional; a two-dimensional periodic orbit in the moon's orbital plane is referred to as a Lyapunov orbit [21-22].

Several methods exist for numerically computing libration point orbits (LPOs). The orbits presented here were computed using a Single-Shooting Algorithm [23]. The focus of this project is on using Halo orbits at the L_1 and L_3 points. Figure 2 shows views of Halo orbits around L_1 in 3D and four different planes. Four views of northern Earth-Moon L_3 halo orbits are shown in Figure 3. Orbits at L_3 can be totally planar (e.g., Lyapunov orbits), or have a very large vertical component. Additionally, certain orbits at L_3 actually have perigees that are less than the geosynchronous radius (42,184 km).

D. Stability of Libration Points and Halo Orbits

To determine the stability of the libration points, a perturbed displacement is defined and substituted into the equations of motion which are then Taylor-expanded up to linear terms about (x_e, y_e, z_e) . Evaluating the characteristic equations for the collinear Lagrange points (L_{1-3}) reveals their saddle-type instability while L_{4-5} maintain linear stability. For the L_1 libration point in the Earth-Moon system, the eigenvalues are $\lambda = \pm 2.9321, \pm 2.3344i, \pm 2.2688i$ which correspond to the E^S , E^U , and E^C subspaces, respectively. For the L_3 libration point in the Earth-Moon system, the eigenvalues are $\lambda = \pm 0.7548, \pm 1.0038, \pm 1.8914i$. To obtain the stability of halo orbits, Floquet theory must be used. The monodromy matrix is defined as the state transition matrix computed at the orbital period, and its eigenvalues (Floquet multipliers) can be used to obtain a stability index. A stable orbit has a stability index of one, and stability indices greater than one corresponds to unstable orbits. As the stability index increases, the orbital stability decreases. Halo orbits at L_1 and L_2 can have stability indices that vary greatly, depending on their size and proximity to the secondary. For example, in the Earth-Moon system, a family of simple L_1 halo orbits can have stability indices that range from 1 to over 1000. However, halo orbits at L_3 are relatively much more stable, with stability indices ranging from 1 to 1.382. For periodic orbits in the CRTBP, it is useful to introduce the parameter τ , which is used to describe the position of a particle on a periodic orbit. This is similar to the mean anomaly in the two-body problem, and is therefore a measure of the time elapsed on the periodic orbit and not an angular measurement. The value of τ ranges from 0-360 degrees, increasing in the

direction of orbital motion. τ is defined to be zero at the orbit's initial x-axis crossing in the +y direction, and -180 at the x-axis crossing in the -y direction, as shown in Figure 4.

E. Invariant Manifolds

Stable (unstable) manifolds consist of the set of all possible trajectories a spacecraft could follow as it asymptotically approaches (departs) a libration point. The nonlinear stable (W^s) (unstable (W^u)) manifolds can be found by numerically integrating the CR3BP equations with an initial condition of the state of each libration point orbit perturbed in the direction of its stable (unstable) eigenvector backward (forward) in time. The size of perturbation applied to produce the stable (unstable) manifolds in Earth-Moon system is 10^{-4} in non-dimensional units. The stable and unstable manifolds of a L_1 halo orbit can be seen in Figure 5 as tube-like structures. Each orbit has two associated stable and unstable manifold sets: one corresponding to a positive perturbation, and one corresponding to a negative perturbation. The stable and unstable manifolds of periodic orbits can be found at any point along the orbit. To find the manifolds at each point along the orbit, it is first necessary to propagate the stable and unstable eigenvectors to the desired position along the orbit using the state transition matrix. The unstable (stable) manifold for a periodic orbit can be calculated by propagating a state perturbed in the unstable (stable) direction forward (backward) in time. The stability of an orbit dictates how fast a particle can travel through the manifolds. Orbits with a lower stability index (more stable orbits) have stable (unstable) manifolds which takes longer time for a particle to get close (far) to the periodic orbit. As a comparison, stable manifolds of two LPOs around L_1 , one with $v=2.7$ and the other with $v=1031.3$, have been propagated for 75 days in Figure 6. The stable manifold of the more unstable LPO gets close the vicinity of the Earth, but the manifold corresponding to the one with lower stability index is still in the vicinity of LPO. Halo orbits around L_3 are much more stable then the halo orbits around L_1 (the stability index for L_3 Halo orbits are less than 1.4); therefore, the related manifolds for L_3 halo orbits are much slower and it takes very long times to get close to L_3 halo orbits using these trajectories. Figure 7 shows that for stable manifolds of L_3 halo orbits, after one year propagation there are few perigees less than 20,000 km and after two year propagation there are some perigees less than 20,000 km which all occur after 540 days of propagation. As a result of this study, it was found that invariant manifolds are not practical to design trajectories for transfers to L_3 halo orbits.

F. Pseudo-Manifolds

In order to take advantage of the convergent/divergent behavior of manifolds and construct transfer trajectories from Earth which will arrive to the orbit in a reasonable time frame, the concept of a Pseudo-Manifold was introduced in the first year of the project. The Pseudo-Manifold varies from the traditional manifold in two distinct ways:

- 1) The perturbation to construct the trajectory is only given to the velocity components of the state, and
- 2) the magnitude of the perturbation is much larger (1000 times larger than the perturbation needed to produce the true manifolds). Figure 8 illustrates the difference between the stable manifold and the pseudo-stable manifold for a L_3 halo orbit with Jacobi Constant $C = 2.4207$. The location on the orbit to give the perturbation for producing the manifold trajectories was selected as $\tau = 17$. The applied perturbation (ϵ) for the stable manifold is 10^{-4} in non-dimensional units, and for the pseudo-stable manifold, $\epsilon = 130 \text{ m/s} = 0.1269$ non-dimensional units. The stable manifold trajectory was propagated for

312 days while the pseudo-stable manifold trajectory was propagated for only 48 days. The pseudo-stable manifold, however, quickly departs the vicinity of the halo orbit and performs flybys of both the Earth and the Moon. Over the given time frames, the perigee of the stable manifold is 74,454 km and occurs on day 293 of the trajectory while the pseudo-stable manifold has a perigee of 7,056 km on day 46 of the trajectory.

G. Earth Coverage and GEO Surveillance from Libration Point Orbits

Another goal of this project is to study the visibility of the Earth's surface as well as the geosynchronous (GEO) belt using a constellation of spacecrafts in halo orbits about the L_1 and L_3 libration points. Space-Based Space Surveillance (SBSS) is essential to improve and maintain our knowledge of the many objects in space such as debris and other spacecraft. Unlike the LEO and GEO regions, there is no other spacecraft in Earth-Moon halo orbits and consequently there is no danger of collision with orbital debris and reduced risk of intentional interference. Also, SBSS is not affected by weather or the time of day, so it can record useful data more consistently than ground-based systems. Furthermore, because observations made from space do not have an atmosphere diffusing what little light is available, SBSS has the potential to see dimmer objects. Past SBSS missions have used telescopes in sun-synchronous orbits [15]. SBSS has been proven useful by many studies and multiple delivered spacecraft. Some notable examples are the U.S. Air Force's Space-Based Visible (SBV) sensor on the MSX spacecraft, the Space-Based Space Surveillance (SBSS) Block 10 System built by Boeing and Ball Aerospace [26], and the Canadian Sapphire satellite [27]. The SBV sensor was part of the first system to perform SBSS [28].

Summary of the Most Important Results

A. Optimal Transfers to L_1 , L_3 , and L_1 Halo Orbits

Two optimization methods were used for finding minimum-fuel manifold-based co-planar transfers to L_1 and L_3 : a grid search and a genetic algorithm. The grid search optimization method is a direct search type algorithm that can be computationally inexpensive when the number of variables in the cost function is minimal [29]. In this method, a grid is constructed in the decision space and the cost function is evaluated at each grid point. The decision space includes all possible values of each variable. The grid point that minimizes the ΔV_{total} is therefore the optimal solution. The variable θ is assumed to vary from 0 degrees to 359 degrees by increments of 1 degree. The resulting optimal trajectory for transfer from a 300 km LEO to L_1 occurs at $\theta=3^\circ$ with $\Delta V_{\text{total}}=3.72$ km/s and a time of flight of 24.8 days, while the optimal trajectory to the L_3 point takes 155.9 days with $\Delta V_{\text{total}}=3.49$ km/s and $\theta=3^\circ$.

For finding optimal two-impulse transfer trajectories to a L_1 halo orbit, a specific southern halo orbit with a Jacobi constant of $C=3.10$, stability index of 216.06, period of 12.1 days, and z-amplitudes of 29,714 km and -42,592 km is selected and an initial 300 km LEO or 35,780 km GEO is assumed. This initial orbit is considered to be inclined relative to the Moon's (x-y) orbital plane with a free inclination that is solved for in the optimization process in the case of departing LEO or constrained as 20 deg from the x-y plane in the case of departing GEO, where θ is the departure angle measured counter-clockwise from the x-axis. The initial ΔV for a transfer trajectory that intersects the stable manifold of L_1 or L_3 along with the angle θ are the variables need to be determined through the optimization. A second impulsive maneuver is needed

to change the velocity of the spacecraft so that it matches the velocity of the stable manifold at the intersection point. A minimum distance function is used to find the closest point for which the transfer and manifold intersect, along with the corresponding velocities. By altering the values of each variable, an infinite number of transfers can be produced to simulate the transfer of a spacecraft from LEO to the L_1 or L_3 stable manifold. A combination of a genetic algorithm (GA), primer vector theory, and a level I differential corrector were used to solve for the free variables that produce an optimal two-impulse low-cost transfer, where the population is described by four variables: the point on the halo orbit from which the stable manifold is propagated (τ), the time the manifold is propagated for (t_s), the pseudo right ascension to the ascending node (pseudo- Ω , defined relative to the x-y plane), and the total delta-v, which is the dependent variable. The target position on the stable manifold is the final point after which it has been propagated for time t_s . Primer vector theory is then used in the fitness function to determine the optimal departure point from LEO or GEO by allowing for an initial coast that improves the cost function. The GA continues for 100 generations or until there has been no improvement in the dependent variable for ten generations.

The optimal trajectories obtained by this method are shown in Figs. 9-10, in which the GA scatter plots are shown converging to the optimal solution. In Fig. 9 for LEO departure the ΔV_{total} for this transfer is 3.61 km/s with a $\Delta V_1 = 3.07$ km/s and $\Delta V_2 = 0.54$ km/s. This transfer is described by its τ value of 198 deg, pseudo- Ω of 155.07 deg, and a t_s of 34.68 days. The algorithm found an optimal initial LEO inclined 21.82 deg relative to the Moon's orbital plane while the time of flight is 37.93 days. In Fig. 10 for GEO departure the ΔV_{total} for this transfer is 1.14 km/s with a $\Delta V_1 = 0.89$ km/s and $\Delta V_2 = 0.25$ km/s. This transfer is described by its τ value of 280 deg, pseudo- Ω of 176.03 deg, and a t_s of 35.64 days. The time of flight is 40.75 days. By comparison, direct transfers and alternative locally optimal transfers from LEO and GEO are shown in Figs. 11-12, respectively. The direct transfer from LEO requires a ΔV_{total} of 3.77 km/s, which is 160 m/s more than that for the optimal transfer. However, the direct transfer takes only 3.82 days. On the other hand, a locally optimal transfer that requires less travel time and a small amount of extra delta-v is shown where $\Delta V_{\text{total}} = 3.63$ km/s and the transfer time is 29.56 days. The direct transfer from GEO requires a ΔV_{total} of 1.44 km/s, which is 300 m/s more than that for the optimal transfer. However, the direct transfer takes only 5.12 days. On the other hand, a locally optimal transfer that requires less travel time and a small amount of extra delta-v is shown that requires 10 fewer days than the globally optimal transfer and requires 50 m/s more in ΔV_{total} .

B. Analysis of Thrust Dispersion Effects

Thrust dispersion analyses for the manifold injection maneuvers (assuming impulsive burns) were examined for the L_1 halo orbit optimal transfer discussed above. Monte Carlo analyses of 1000 simulations each were performed with effects of thrust magnitude and direction errors analyzed separately and in combination on the resulting miss distance and transfer times. Gaussian dispersions for the same three errors are introduced into the system: one for the ΔV_2 magnitude (assuming 1σ for 1% error) and two for the ΔV_2 direction in the burn-plane and out-of-plane directions (assuming 1σ for 1 degree error). The results shown in Figs. 13-14 for departure from LEO and GEO, respectively, illustrate the need for a guidance scheme to mitigate the effects of thrust errors. For the combined thrust magnitude and

direction errors with LEO departure, the mean miss distance was 17678.06 km with a 1σ of 3196.48 km while the transfer times had a mean of 22.22 days with a 1σ of 1.66 days. For the combined thrust magnitude and direction errors with GEO departure, the mean miss distance was 6884.71 km with a 1σ of 2583.56 km while the transfer times had a mean of 23.50 days with a 1σ of 0.77 days. Note the presence of outliers in the miss distance dispersions representing trajectories that completely miss the halo orbit by thousands of kilometers. These large final position errors at the halo orbit insertion point do not allow a ballistic transfer as desired.

C. LQR-Based Continuous Thrust Guidance

A neighboring optimal guidance scheme based on the linear quadratic regulator (LQR) was implemented assuming the spacecraft has a mechanism for low continuous thrust during its travel time on the stable manifold in order to correct for the thrust dispersion errors and reduce the miss distance at the halo orbit insertion point. The effectiveness of the guidance control for the transfers from LEO and GEO is seen in Figs. 15-16 which shows the transfer plot, position and velocity state differences (as compared with the nominal states on the stable manifold), and the three elements of the control input vector. For the LEO departure case with guidance in Figure 15, the guided position and velocity deviations which are now significantly reduced. The final miss distance is 3.05 m, a significant improvement over the cases of transfer without guidance and the optimal transfer without any injection errors. This shows that small targeting errors that lead to significant miss distances can be compensated for with the guidance scheme. The guidance controller uses a total Δv of 15.365 m/s during its 34.57 day trip on the manifold. It can be seen that there is large control magnitude immediately after the Δv_2 maneuver which quickly decays for the rest of the transfer. The maximum output thrust used in this control scheme for this transfer is 100.0067 m/s². This thrust output is feasible with the currently existing low-thrust engines. For the GEO departure case with guidance in Figure 16, the final miss distance is 1.96 m. The guidance controller uses a total Δv of 7.052 m/s during its 35.64 day trip on the manifold. The maximum output thrust used in this control scheme for this transfer is 0.003042 m/s². Again, this output thrust is feasible with currently existing low-thrust engines. Finally, we repeat the GEO departure case while limiting the thrust magnitude used in the guidance scheme to a maximum of $T_m = 0.01$ mm/s². Figure 17 shows the corresponding results which show that the state deviations from those on the manifold are still reduced to zero but over a longer period than in Fig. 16. The final miss distance in this case is 2.5 m while the controller uses a total Δv of 12.795 m/s during its 35.64 day trip on the manifold. It is noticed that the cost is increased from the case without thrust limits.

D. Impulsive Guidance

A more realistic guidance strategy is to use impulsive trajectory correction maneuvers (TCMs) instead of the continuous thrust that results from the LQR-based solution. Our impulsive guidance strategy utilizes the state transition matrix (STM) to propagate state deviations. Two impulsive TCMs (constituting a “burn pair”) are used: the first burn at time t_1 re-targets the manifold and the second burn at time t_2 corrects the velocity error upon arrival at the manifold. Control strategies include options where only single burns or full burn pairs are implemented. The timing of the TCMs was obtained first by a brute force trial-and-error approach and then by using the Liapunov Exponents (LEs) associated with the halo orbit stable manifold. The LEs associated with the stable manifold portion of the optimal two-impulse transfers in

Figs. 9-10 for departure from LEO and GEO are shown in Figure 18, in which the maximum values correspond to perigees and the minimum values correspond to apogees. The initial hypothesis that the TCMs should be performed at apogee locations (minimum values of LEs) was confirmed through testing multiple ideas on how to use them in implementing the TCM burn times. The resulting transfers from LEO and GEO with single impulsive TCMs calculated from the LEs are shown in Figs. 19-20, in which the thrust errors (1% magnitude and 1 deg in-plane and out-of-plane) are incorporated in the manifold injection maneuver as well as in all subsequent TCMs, which are indicated by the black circles in the transfer plot with the relative magnitudes shown in the plots below. In the case of the transfer from LEO, the miss distance at halo orbit insertion is reduced to 4.858 km while the transfer time is 34.569 days. The delta-v cost for the impulsive guidance is 22.034 m/s. In the case of the transfer from GEO, the miss distance at halo orbit insertion is reduced to 1.092 km while the transfer time is 35.642 days. The delta-v cost for the impulsive guidance is 8.634 m/s. This shows that the impulsive guidance scheme is effective in mitigating the position errors on the stable manifold as well as the halo insertion miss distance that result from thrust errors in the manifold injection maneuver and the TCMs themselves compared to the case where no guidance is used.

E. Optimal Mixed Impulsive/Continuous Thrust Transfers to L_1 Liapunov Orbits

Optimal transfer trajectories were designed for a spacecraft using mixed impulsive and continuous thrust propulsion to depart low-Earth orbit and enter a specified planar Lyapunov orbit at the interior L_1 Earth-Moon Lagrange point in the framework of the planar circular restricted three-body problem. Due to the fact that impulsive and continuous thrust transfers have their own relative advantages and disadvantages, the combination of the two propulsion types has been suggested as a way to combine the benefits of both systems into transfer trajectory designs. The flight time and impulsive/continuous thrust weighting factor are specified in advance, while the results from two separate performance indices based on minimum fuel and minimum control energy were compared. The continuous dynamic optimization problem was reformulated as a discrete optimization through direct transcription and collocation, which then was solved using nonlinear programming software. The optimal transfer trajectory results were analyzed using the Pareto front solutions. Fig. 21 shows direct and spiral departure transfer trajectories and the corresponding control acceleration histories using a quadratic performance index in the optimal control problem (OCP). The results for varying numbers of nodes are shown to illustrate when convergence is achieved: for the direct departure case (which includes a mandatory coast period after the initial impulsive maneuver to depart GEO) 197 nodes is shown to be sufficient while for the spiral departure case 99 nodes is sufficient (for which the control history is smooth). By contrast, Fig. 22 shows direct and spiral departure transfer trajectories and the corresponding control acceleration histories using a minimum fuel performance index for spiral departure in the OCP, in which 99 nodes is shown to be sufficient for convergence and the thrust history consists of two periods of maximum thrust at the pre-set thrust limit (dashed red line) and two periods of coast arcs with no thrust. The bang-off-bang thrust profile was found to be explained in the context of primer vector theory when the performance index minimizes the actual fuel used as opposed to the case of a quadratic performance index.

F. Efficient Transfers to L_3 Halo Orbits

Work has continued on finding efficient transfers from LEO to halo orbits about the Earth-Moon L_3 Lagrange point. Due to very slow nature of the L_3 halo orbit's stable manifolds, Davis et al. [5] proposed transfers based on L_3 halo orbit pseudo-manifolds (defined by applying a large perturbation in the velocity component of the eigenvector) from LEO to lunar L_3 halo orbits to take advantage of the convergent/divergent behavior of manifolds and construct transfer trajectories from Earth which will

arrive to the orbit in a reasonable time frame. For transfer from a 185 km LEO to a northern L3 halo orbit with $C = 2.42$ and period of 27.2 days, Fig. 23 shows a pseudo-manifold-based transfer trajectory found in this way where the insertion point at the halo orbit is given by $\tau = 17.36^\circ$ and the velocity perturbation (also the amount of Δv_2 for the 2-impulse transfer) is $\epsilon = 130$ m/s. The first maneuver is a tangential maneuver of 3.07 km/s and is executed in LEO to inject onto the pseudo-manifold. The total ΔV for this transfer is 3.2 km/s while the total transfer time is 45.8 days. In general the total Δv cost is between 3.17 to 3.28 km/s with flight times between 43 and 84 days. However, the lowest Δv_2 that was reported is not less than 130 m/s.

In such mission designs with two impulsive burns, it is important that, for a given total ΔV , as much as possible should be used for the first burn departing LEO while the second burn should be as small as possible. This way, the amount of fuel the spacecraft should carry to the halo orbit is minimized. For this purpose, recent efforts have investigated alternative strategies that result in more desirable transfers. Using a grid search applied to 360 different points of τ (every one degree) where at each τ location on the halo orbit, the orbit's nominal velocity is perturbed in 32400 different directions, departure from a variety of LEO altitudes is achievable. Figure 24 shows the achievable LEO altitudes that result from a 100 m/s perturbation to the nominal state on an L3 halo orbit. The locations for the perturbations are denoted by their τ value. The halo orbit has a Jacobi constant of $C=2.3981$ and period of 27.13 days. The transfer time was limited to 110 days. Transfers were constructed for each of the trajectories with a LEO altitude less than 400 km. It was assumed that the first maneuver to depart from LEO is a tangential maneuver onto the trajectory in order to minimize the value of ΔV_1 . The total ΔV s of the resulting transfer range between 2.94 and 3.14 km/s. The total ΔV increases as the LEO altitude increases. The trajectories found in the Figure 24 can have a time of flight between 45 to 110 days. Figure 25 shows different families of transfers from a 185 km altitude LEO to the same L3 LPO in which the ΔV_2 , ΔV_{total} , and time of flight (TOF) are indicated for each family. A common feature shared between all families shown in Figure 25 is the inclusion of a lunar flyby with an altitude of a few thousand kilometers, while a feature that distinguishes between different families is the number of the Earth flybys which is a measure for the time of flight ranges between the families of the transfers. The number of the Earth flybys varies between no flybys to three flybys if the time of flight is limited to 120 days. Another interesting observation one can find in Figure 25 is that different families are distinguishable even between categories which have similar ranges of TOF. As an example, families of transfers in Figures b, f, i all have one Earth flyby but their TOF varies between three different ranges: 40 days to 47 days for the first family, 62 to 65 for the families in the Figure f, and 62 to 65 days for the families of the transfers showed in Figure i. The same feature is observable for the families which perform no Earth flyby and those who have two Earth flybys. Figure 26 shows the C_3 energy respect to the halo orbit insertion maneuver for the constructed transfers using colored dots. Different transfers colored from blue to red as their transfer time increases. C_3 varies between -1.9 and -2.18. There is no correlation between C_3 and ΔV_2 and also between C_3 and time of flight, while a distinguishable trend can be found for ΔV_2 and time of flight; as ΔV_2 is decreased the time of flight increases.

The three parameters: ΔV_2 , C_3 energy, and ToF, all effects on the cost and feasibility of the transfers. C_3 effects for the launch vehicle and ΔV_2 effects on the type of engine spacecraft need for the second burn

and also the amount of fuel it needs to carry. Therefore, it is necessary to find a trade-off between these three quantities. A transfer requiring the smallest insertion maneuver into the halo orbit can be constructed. Figure 27 shows such a transfer which the minimum possible $\Delta V_2=15$ m/s for insertion into the halo orbit. This transfer requires an escape energy of $C_3=-2.05$ km²/s² and takes 119.6 days to insert into the halo orbit while performing a lunar flyby and only one Earth flyby. On the other hand a transfer can be designed to have the shortest time of flight. Figure 28 shows this transfer which takes only 31 days for the spacecraft to insert into the L₃ halo orbit. The C₃ escape energy for this transfer is -2.02 km²/s² while it needs 90 m/s burn to insert into the halo orbit.

G. GEO Observability Analysis from Libration Point Orbits

Two steps were defined: Visibility analysis of the GEO belt using Matlab programs, and validation of the results using NASA's Ephemeris model in the orbit analysis software Satellite Tool Kit (STK). As the first step, a study was conducted to find the visibility coverage using several constellations of spacecrafts in L₁ and L₃ Halo orbits of Earth-Moon system. By analyzing various constellations, this study tried to find a balance between coverage and cost to provide coverage for largest percentage of the Earth surface while minimizing the number of spacecrafts in the proposed constellation. There are also some other factors must be considered such as orbit insertion costs, orbit maintenance costs, and link budget considerations. For this purpose, a grid was defined by latitude/longitude points for equal dispersion along a sphere. Then, at each point along the halo orbit, using the line-of-sight criteria, it was determined which points of this grid are visible to spacecraft in halo orbits, and finally four percentages were calculated as a parameters of visibility. These parameters are defined as: Total percentage Visible: The total percent of the Earth's surface visible during one full halo orbital period (assuming no rotation of the Earth); Maximum percentage Visible: The percent of the Earth's surface visible at the optimal viewing location on the orbit; Minimum percentage Visible: The percent of the Earth's surface visible at the worst viewing location on the orbit; Average percentage Visible: The average percentage of the Earth's surface visible during an orbital period. To validate the results of the first step, the analyses used a combination of STK and software written in MATLAB. Libration point orbits were generated in MATLAB and saved as STK ephemeris files. The LPO ephemeris files were then imported into STK using the `stkExternal` propagator. Other satellite orbits, such as sun-synchronous orbits and GEO orbits, were imported into STK using the available catalog of two-line elements (TLEs). Finally, STK's J4Perturbation integrator was used to model any arbitrary orbit that was used apart from catalog orbits.

A grid of 1502 points can be defined by latitude/longitude points for equal dispersion along sphere with $N=4^\circ$ in latitude and $M=7.2^\circ$ in longitude. Then, at each point along the halo orbit, using the line-of-sight criteria, it should be determined which points of this grid are visible to spacecraft in halo orbit and finally a percentage were calculated as a value of visibility. The orbit is propagated for four orbital periods of L₃ orbit (approximately 108 days). 2400 different orbit combinations are tested in this study. With one spacecraft on E-M L₁ halo orbit, approximately 50% of the Earth's surface at a given time can be observed. Most of the E-M L₁ halo orbits provide similar coverage characteristics and If the Earth were fixed (i.e., no rotation), less than 60% of the Earth's surface could be seen in 1 full halo period; therefore, Halo orbits at L₁ can only see the "near side" of the Earth. Figure 29 shows the four percentage parameter for a spacecraft on L₁ halo orbit. Also, a spacecraft on L₃ halo orbit, on average, can see over 97% of the

geosynchronous region and there is only small blockage due to Earth. Figure 30 illustrates the maximum amount of geosynchronous region visible during 1 orbital period in green color (best case) and the minimum amount of the geosynchronous region visible during 1 orbital period (i.e., the portion blocked by the Earth) as the worst case. Different constellation like four different combinations of two spacecrafts in two different orbits (1 s/c in L3 orbit (Northern or Southern) and 1 s/c in L₁ orbit (Northern or Southern)) was examined and finally with a constellation of two spacecraft in L3 halo orbit (one in a northern and another in a southern one) and one spacecraft in a northern L₁ halo orbit, there can be a coverage of up to 99.8 percent of Earth surface (as seen in Figure 51) and all examined constellations can see at least 97% of Earth surface on average.

To generate the halo orbit in STK, first, an approximate orbit was generated using a single-shooting algorithm in the Circular Restricted Three-Body Problem. The approximate orbit was converted into a continuous, ballistic trajectory in the high-fidelity model of the solar system using a multiple-shooting differential corrector [18-19]. The high-fidelity model uses the gravity of the Sun, Moon, and all planets, modeled as point-masses traveling in orbits approximated by the Jet Propulsion Laboratory's Planetary and Lunar Ephemerides DE405 [20]. No assumptions were made regarding solar radiation pressure due to the early analyses of these trajectories, but the trajectories will be adjusted in future analyses to compensate for solar radiation pressure. Figure 32 illustrates the L₁, L₂, and L₃ trajectories used in the analyses presented here. The brute force analysis was performed for an observing spacecraft orbiting about L3. Looking at the whole set of possible orbits, we see some interesting patterns appear in Figure 33. At low altitudes, the target spacecraft is visible for an extremely small percentage of the total time. Above 5,000 km, the viewing opportunities become much more abundant, but there are only a few orbits of interest above that point – namely, GPS and GEO. At high altitudes, the limiting factor for target visibility is the phase angle – the viewer only sees the illuminated side of the target about 22.2% of the time. This follows from the assumption made that the phase angle must be less than 40° for visibility ($80^\circ/360^\circ = 22.2\%$). The range of altitudes that houses the GPS, GLONASS, and Galileo navigation constellations is sparsely populated, so GEO emerges as the best orbital regime for observation from a libration-point orbit. Figure 33, Figure 34, and Figure 35 summarize these findings. It was observed that for low-altitude orbits, the visibility was severely affected by the Earth being either directly in front of or directly behind the target satellite. LEO spacecraft also spend much more time in eclipse than higher orbits, resulting in the limited time visible seen above in Figure 32. The effect of each constraint as a function of altitude is shown below in Figure 36.

To examine the visibility of GEO from a LPO, a complete analysis was run independently for observer spacecraft at L₁, L₂, and L₃. Figures 37, 38, and 39 show the percentage of GEO spacecraft that are visible from an L₁, L₂, and L₃ orbit over time, respectively. Figure 40 shows the percentage of the total number of accesses that are shorter than a given duration. Figure 41 is a histogram showing the frequency of various access durations. There are two main spikes in the number of access durations for L₁: one at approximately 2.25 hours and one between 11-12 hours. Figure 42 and Figure 43 demonstrate the frequency of different gap durations. The vast majority of gaps in visibility from L₁ are less than 1 hr (mainly caused by eclipses and the Earth blockage constraint), but there are also quite a few gaps in the 500-600 hour range (caused by the phase angle constraint). The same analysis have been done for GEO visibility from lunar L2 (Figure

44-47) and L3 (Figure 48-51) halo orbit. The visibility from L_2 is almost identical to L_1 . The only difference between the L_1 and the L_2 observers is the distance and because L_2 is further away from the Earth and the GEO belt than L_1 , an observer at L_2 would require a slightly more sensitive optical system.

Figure 48 and Figure 49 show the percentile breakdown of access and gap durations from an L_3 orbit. The blue line marks the percentage of accesses or gaps that are less than a given duration, and the red line marks the mean access or gap duration. The histogram and percentile breakdown show the same data in different ways. We can see that, for both accesses and gaps, the mean value is not very useful. There are a great deal of short gaps and accesses, but the long duration gaps and accesses give us a more accurate representation of a “typical” time period. The many short gaps are caused by restrictions from the Earth angle. Roughly 28% of the gaps are less than 70 minutes, the maximum time a GEO spacecraft would be in eclipse. The longer gaps, which are less frequent, are caused by restrictions from the phase angle. As seen in the figure, these long gaps can last on the order of hundreds of hours. The average gap duration is 146 hr. The access duration has a similar trend to gap duration, with many short accesses and fewer long accesses that can last for hundreds of hours. The average access duration is 42 hr.

Another important consideration for optical observations is the distance between the target and the observer. The distance varies considerably for an observer in L_3 , with a broad distribution from 1×10^5 km to 6.5×10^5 km. Such a broad range of distances between sensor and target complicates telescope design, as it must be capable of varying its focusing distance by nearly an order of magnitude to image everything. However, it is important to remember that the longer accesses (which make up the vast majority of total access time and are thus more desirable) occur when the distance between spacecraft is largest (when the L_3 spacecraft is at apogee). Therefore, it may be possible to capture most of the total access time by limiting the focal distance range to $5 \times 10^5 - 6 \times 10^5$ km.

H. Earth Observability Analysis from Libration Point Orbits

Two steps were defined: Visibility analysis of the Earth surface using Matlab programs, and validation of the results using NASA's Ephemeris model in the orbit analysis software Satellite Tool Kit (STK). To compute cumulative visibility, the Earth's rotation is modeled using the following assumptions: Earth's North Pole is always aligned with the z-axis in the CRTBP, Earth completes a rotation in one sidereal day (86164.09056 seconds), and 0 deg longitude is on the x-axis pointing towards the Moon at the scenario epoch. Twenty five hundred locations were selected on the halo orbit, each equidistant in time. At each time step, line of sight visibility was computed for all points on the latitude/longitude grid. Figure 52 shows the average visibility for two northern L_1 halo orbits during an orbital period. The most planar orbit, Figure 52(a) provides more uniform coverage of all latitudes while the most vertical orbit, Figure 52(b), provides better coverage of the North Pole. Figure 53 shows the average visibility of points on the Earth for three northern L_3 halo orbits during one orbital period. Each halo orbit in the sequence (a, b, c) becomes increasingly planar and more uniform coverage at all latitudes is achieved. Figures 52 and 53 show that coverage is nearly constant for a given latitude. Thus, the next step in the analysis is to compute the average visibility for each latitude for a variety of halo orbits. For each halo orbit, the average visibility of each latitude is plotted with respect to the orbit's initial x-condition, as shown in Figure 54. For STK validation, an example northern L_1 orbit with $A_z = 45,500$ km and an example southern L_3 orbit with $A_z = 127,800$ km were selected. Earth surface coverage was computed at a variety of ephemeris epochs. The epochs were chosen in order to analyze the effects of the lunar rotational period (approximately 27.32

days) and the lunar nodal cycle (approximately 18.6 years). Figures 55 and 56 show the average visibility by latitude for one halo orbiter at L1 and L3, respectively. The subplots (a), (b), (c), and (d) reflect the lunar nodal cycle; during the years 2015, 2020, 2025, and 2029, the Moon's right ascension of the ascending node with respect to the Earth is approximately 180, 90, 0, and 270 deg, respectively. For each year, sixteen epochs were selected. Each subsequent epoch was 6.83 days (one-fourth of the lunar rotational period) after the previous. Thus, Epoch 2 is 6.83 days after Epoch 1 and so forth. For reference, the nominal coverage computed in the CRTBP is also shown in each subplot. Also note that the orbit's initial state in the CRTBP is on x-axis with positive y-velocity. Figures 55 and 56 show that the average coverage by latitude approximately repeats every fourth epoch, correlating to the lunar rotational period. The variations between every fourth epoch are slightly larger for L1 orbits than for orbits at L3.

Also, coverage is computed for single satellites and constellations of spacecraft in halo orbits about L1 and L3. The goal is to achieve the highest surface coverage using a minimum number of spacecraft. Constellations considered include a two-spacecraft constellation with one L1 orbiter and one L3 orbiter, a three-spacecraft constellation with one L1 orbiter and two L3 orbiters in mirrored northern and southern orbits, and a four-spacecraft constellation with two L1 orbiters and two L3 orbiters. Figures 57 and 58 show the average percent visibility of the Earth's surface by at least one spacecraft and average percent visibility at each latitude for the constellations that provide the best and worst coverage. For STK validation, the orbits that provided the best coverage were analyzed in STK for the epochs used in the single-spacecraft coverage analysis. For the three-spacecraft constellation the coverage from the full ephemeris is compared with that from the Matlab analysis in Fig. 59. Similar to the coverage provided by one orbiter, Fig. 59 shows that the average coverage by latitude approximately repeats every fourth epoch for the constellation while the variations between different epochs are on a much smaller scale. It is also observed that the coverage in the ephemeris is better at the poles than in the Matlab analysis of the circular restricted three-body problem. Still, the CR3BP is a reasonably good model for the coverage that can be expected in the ephemeris. Furthermore, the fact that certain L3 southern orbits may provide more coverage of the Northern hemisphere is nullified by the fact that two reciprocal orbits are used at L3 for the constellation.

Bibliography

- [1] Larsen, W. Anthony, T. Critz, M. Nazari, M. Deilami, E. Butcher, G. Born, and J. McMahon, "Optimal Transfers with Guidance to the Earth-Moon L_1 and L_3 Libration Points using Invariant Manifolds: A Preliminary Study," Proc. 1012 AAS/AIAA Astrodynamics Specialist Conference, Minneapolis, MN, 2012.
- [2] K. E. Davis, G. H. Born, M. Deilami, A. Larsen, and E. A. Butcher, "Transfers to the Earth-Moon L_3 Halo Orbits," Proc. 1012 AAS/AIAA Astrodynamics Specialist Conference, Minneapolis, MN, 2012.
- [3] Anthony, W., Larsen, A., and Butcher, E. A., "Optimal Impulsive Manifold-Based Transfers with Guidance to L1 Halo Orbits," 2013 AAS Spaceflight Mechanics Conference, Kauai, HI, Feb. 10-14, 2013.
- [4] Lee, D. Butcher, E. A., and Sanyal, A. K., "Optimal Mixed Impulsive/Continuous Thrust Trajectories to the Interior Earth-Moon L_1 Lagrange Point," 2013 AAS Spaceflight Mechanics Conference, Kauai, HI, Feb. 10-14, 2013.

- [5] Parrish, N., Parker, J., Bradley, B., "GEO Observability from Earth-Moon Libration Point Orbits," 2013 AAS Spaceflight Mechanics Conference, Kauai, HI, Feb. 10-14, 2013.
- [6] Anthony, W., Larsen, A., Butcher, E. A., and Parker, J., "Impulsive Guidance for Optimal Manifold-Based Transfers to Earth-Moon L1 Halo Orbits," 2013 Astrodynamics Specialist Conference, Aug. 11-15, Hilton Head, SC.
- [7] Davis, K., Parrish, N., Born, G.H., and Butcher, E.A., "Earth Coverage from Earth-Moon Libration Point Orbits," 2013 Astrodynamics Specialist Conference, Aug. 11-15, Hilton Head, SC.
- [8] Davis, K. E., Butcher, E. A., Parker, J. S., and Deilami, M. Z., "Improved Transfers to Earth-Moon L3 Halo Orbits," AAS 14-236, 2014 AAS Spaceflight Mechanics Meeting, Jan. 26-30, 2014, Santa Fe, NM.
- [9] Anthony, W., Butcher, E. A., and Parker, J., "Statistical Fuel Budgets for Impulsive Guidance to Earth-Moon L1 Halo Orbits," 2014 Astrodynamics Specialist Conference, Aug. 4-7, 2014, San Diego, CA.
- [10] Nazari, M., Anthony, W., and Butcher, E. A., "Continuous Thrust Stationkeeping in Earth-Moon L1 Halo Orbits Based on LQR Control and Floquet Theory," 2014 Astrodynamics Specialist Conference, Aug. 4-7, 2014, San Diego, CA.
- [11] Davis, K., Born, G., and Butcher, E.A., "Transfers to Earth-Moon L₃ Halo Orbits," *Acta Astronautica*, doi: 10.1016/j.actaastro.2013.03.004 (2013).
- [12] Lee, D. Butcher, E. A., and Sanyal, A. K., "Optimal Interior Earth-Moon Lagrange Point Trajectories using Mixed Impulsive and Continuous Thrust," *Aerospace Science and Technology*, submitted.
- [13] Larsen, A., Butcher, E. A., and Born, G., "Optimal Impulsive Manifold-Based Transfers to Earth-Moon L1 Halo Orbits," in preparation.
- [14] Anthony, W., Butcher, E. A., Parker, J., McMahon, J., and Born, G., "Continuous and Impulsive Guidance with Statistical Fuel Budgets to Earth-Moon L1 Halo Orbits," in preparation.
- [15] Butcher, E. and Nazari, M., "Optimal Control of Spacecraft Motion in Time-Periodic Astrodynamical Systems," extended abstract for 8th European Nonlinear Dynamics Conference, July 6-11, 2014, Vienna.
- [16] Butcher, E., "Comparison of Strategies for Control of Time-Periodic Astrodynamical Systems," invited talk at Air Force Research Laboratory, Albuquerque, NM, July 30, 2013.
- [17] V. Szebehely, *Theory of Orbits: The Restricted Problem of Three Bodies*. New York: Academic Press, 1967.
- [18] R. A. Broucke, "Periodic Orbits in the Restricted Three-Body Problem with Earth-Moon Masses," Tech. Rep. 32-1168, Jet Propulsion Laboratory, Cal. Tech., 1968.

- [19] R. W. Farquhar and A. A. Kamel, "Quasi-Periodic Orbits about the Translunar Libration Point," *Celestial Mechanics*, Vol. 7, June 1973, pp. 458-473.
- [20] J. V. Breakwell and J. V. Brown, "The Halo Family of 3-Dimensional Periodic Orbits in the Earth-Moon Restricted 3-Body Problem," *Celestial Mechanics*, Vol. 20, November 1979, pp. 389-404.
- [21] G. Gomez, A. Jorba, J. Llibre, R. Martinez, J. Masdemont, and C. Simo, *Dynamics and Mission Design near Libration Points*, Vol. I-IV. Singapore: World Scientific Publishing Co., 2001.
- [22] M. Henon, "New Families of Periodic Orbits in Hill's Problem of Three Bodies," *Celestial Mechanics and Dynamical Astronomy*, Vol. 85, 2003, pp. 223-246.
- [23] K.C. Howell, and H.J. Pernicka, "Numerical Determination of Lissajous Trajectories in the Restricted Three-Body Problem," *Celestial Mechanics*, Vol. 41, Nos. 1-4, 1988, pp. 107-124.
- [24] R. W. Farquhar, "Lunar Communications with Libration-Point Satellites," *Journal of Spacecraft and Rockets*, Vol. 4, No. 10, 1967, pp. 1383-1384.
- [25] K. C. Howell, "Three-Dimensional, Periodic, 'Halo' Orbits," *Celestial Mechanics*, Vol. 32, No. 1, 1984, pp. 53-71.
- [26] The Boeing Company. Space Based Space Surveillance (SBSS) System Mission Book. <http://www.boeing.com/defense-space/space/satellite/MissionBook.pdf> (accessed July 12, 2012).
- [27] Maskell, P. and Oram, L. "Sapphire: Canada's Answer to Space-Based Surveillance of Orbital Objects," Advanced Maui Optical and Space Surveillance Technologies Conference, Maui, 2008.
- [28] Utmann, J. "Space-Based Space Surveillance as Complementary Element in an SSA Architecture," European Space Surveillance Conference, Madrid, Spain, 2011.
- [29] D. N. Kumar, "Advanced Topics in Optimization: Discrete and Indirect Search Methods," Indian Institute of Science.
- [30] Parker, J. *Low-Energy Ballistic Lunar Transfers*; Ph.D. Thesis; University of Colorado: Boulder, Colorado, 2007.
- [31] Wilson, R. S. and Howell, K. C., "Trajectory Design in the Sun-Earth-Moon System Using Lunar Gravity Assists," *Journal of Spacecraft and Rockets*, Vol. 35, No. 2, 1998, pp. 191-198.
- [32] Standish, E. M. *JPL Planetary and Lunar Ephemerides, DE405/LE405*; IOM 312.F-98-048; California Institute of Technology, August 1998.

List of Figures

- Figure 1. Circular Restricted Three Body Problem in non-dimensional frame
- Figure 2. Several example orbits from the family of halo orbits about the Earth-Moon L1 point.
- Figure 3. Several example orbits from the family of halo orbits about the Earth-Moon L3 point.
- Figure 4. Values of τ around a periodic orbit.
- Figure 5. Stable (green) and unstable (red) exterior manifolds of an L1 halo orbit.
- Figure 6. Stable manifold trajectories of two L1 LPOs with significantly different stability coefficients
- Figure 7. The perigees of WS trajectories of an L3 halo orbit with $C=2.42$ propagated for one year (left) and two years (right). The color of the marker indicates the day on which perigee occurs.
- Figure 8. Planar views of the stable (left) and pseudo-stable (right) manifold trajectories which depart from the same location on the nominal L3 halo orbit.
- Figure 9. Optimal two-impulse transfer from LEO to a southern L1 halo orbit with $C=3.10$. Delta- v_2 is indicated by the pink circle. The genetic algorithm scatter plot is shown converging to the optimal solution.
- Figure 10. Optimal two-impulse transfer from GEO to a southern L1 halo orbit with $C=3.10$. Delta- v_2 is indicated by the pink circle. The genetic algorithm scatter plot is shown converging to the optimal solution.
- Figure 11. Direct and an alternative locally optimal transfer from LEO to a southern L1 halo orbit with $C=3.10$. Delta- v_2 is indicated by the pink circle.
- Figure 12. Direct and an alternative locally optimal transfer from GEO to a southern L1 halo orbit with $C=3.10$. Delta- v_2 is indicated by the pink circle.
- Figure 13. Effects of thrust magnitude and direction dispersions at manifold injection on miss distance and transfer times without guidance for LEO transfers. Miss distance dispersions are for thrust errors in magnitude, in-plane direction, out-of-plane direction, and all three combined.
- Figure 14. Effects of thrust magnitude and direction dispersions at manifold injection on miss distance and transfer times without guidance for GEO transfers. Miss distance dispersions are for thrust errors in magnitude, in-plane direction, out-of-plane direction, and all three combined.
- Figure 15. LQR-based guidance with manifold injection errors for L1 halo orbit transfer from LEO.
- Figure 16. LQR-based guidance with manifold injection errors for L1 halo orbit transfer from GEO.
- Figure 17. LQR-based limited thrust guidance ($T_m = 0.01 \text{ mm/s}^2$) with manifold injection errors for L1 halo orbit transfer from GEO.
- Figure 18. Liapunov exponents for the L1 halo orbit stable manifold associated with the optimal transfers from LEO and GEO in Figs. 9-10.
- Figure 19. Impulsive guidance with manifold injection and TCM thrust errors using LEO departure.
- Figure 20. Impulsive guidance with manifold injection and TCM thrust errors using GEO departure.
- Figure 21. Direct and spiral departure transfer trajectories from GEO to a L1 Liapunov orbit with corresponding continuous thrust magnitudes using mixed impulsive and continuous thrust and quadratic performance index in the OCP.

Figure 22. Direct and spiral departure transfer trajectories from GEO to a L1 Liapunov orbit with corresponding continuous thrust magnitudes using mixed impulsive and continuous thrust and minimum fuel performance index in the OCP.

Figure 23. A pseudo-manifold-based transfer trajectory from a 185 km LEO to an L3 halo orbit with $C = 2.40207$.

Figure 24. Perigee altitudes (km) for different trajectories with respect to the insertion point into the L3 halo orbit, where $\Delta v_2 = 100$ m/s.

Figure 25. Different families of transfers from a 185 km altitude LEO to the L3 halo orbit.

Figure 26. C_3 energy for the departing maneuver with respect to the insertion maneuver into the halo orbit. The color bar shows the flight times in days.

Figure 27. Transfer trajectory to the L3 halo orbit which has the smallest possible insertion maneuver. $C_3 = -2.05 \text{ km}^2/\text{s}^2$, $\Delta V_2 = 0.015 \text{ km/s}$, TOF = 119.6 days.

Figure 28. Transfer trajectory to the L3 halo orbit which has the least possible time of flight. $C_3 = -2.02 \text{ km}^2/\text{s}^2$, $\Delta V_2 = 0.09 \text{ km/s}$, TOF = 31 days.

Figure 29. Visibility of Earth surface using a spacecraft on L₁ halo orbit

Figure 30. Visibility of geosynchronous orbit using a spacecraft on L₁ halo orbit

Figure 31. Average percentage of Earth surface visibility by one or more satellites in a constellation of two satellites in L₃ halo orbit and one on L₁ halo orbit

Figure 32. Screenshot of STK showing the L₁, L₂, and L₃ libration point orbits used in the analyses presented here and illustrated in the Earth-Moon rotating coordinate frame.

Figure 33. Portion of time where target is visible for various altitudes and inclinations

Figure 34. Mean access duration for various altitudes and inclinations.

Figure 35. Mean gap duration for various altitudes and inclinations.

Figure 36. Effect of each constraint on percent time visible for the LEO and MEO regimes.

Figure 37. Percentage of GEO spacecraft visible from L₁ over time

Figure 38. Percentage of GEO spacecraft visible from L₂ over time

Figure 39. Percentage of GEO spacecraft visible from L₃ over time

Figure 40. Breakdown of access durations from L₁.

Figure 41. Histogram of access durations from L₁

Figure 42. Breakdown of gap durations from L₁

Figure 43. Histogram of gap durations from L₁

Figure 44. Breakdown of access durations from L₂.

Figure 45. Histogram of access durations from L₂

Figure 46. Breakdown of gap durations from L₂

Figure 47. Histogram of gap durations from L₂

Figure 48. Breakdown of access duration from L₃.

Figure 49. Histogram of access durations from L₃.

Figure 50. Breakdown of gap duration from L₃.

Figure 51. Histogram of gap durations from L₃.

Figure 52. Percent visibility for latitude/longitude points on the Earth surface for selected northern L1 halo orbits assuming Earth's spin axis is identified with z-axis of CR3BP.

Figure 53. Percent visibility for latitude/longitude points on the Earth surface for selected northern L3 halo orbits assuming Earth's spin axis is identified with z-axis of CR3BP.

Figure 54. Average Earth visibility by latitude for northern L1 and L3 halo orbits.

Figure 55. Average visibility by latitude at different ephemeris epochs for an L1 orbiter from STK analysis.

Figure 56. Average visibility by latitude at different ephemeris epochs for an L3 orbiter from STK analysis.

Figure 57. Average percent visibility of the Earth's surface by at least one spacecraft in a constellation of a) two spacecraft and b) three spacecraft in L1 and L3 LPOs.

Figure 58. Average percent visibility at each latitude for the constellations that provide the best and worst coverage in a constellation of a) two spacecraft and b) three spacecraft.

Figure 59. Visibility by latitudes at different ephemeris epochs for a three-spacecraft constellation: comparison of STK analysis (Epochs 1-16) with the nominal CR3BP analysis.

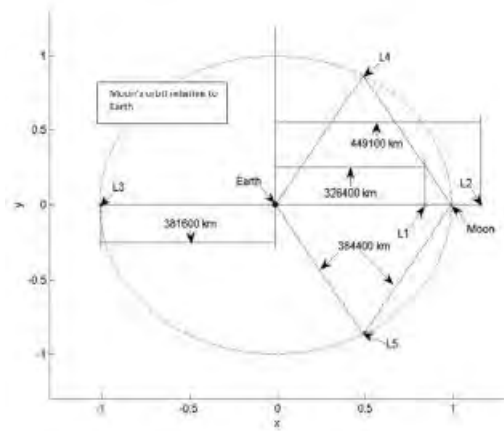


Figure 1-Circular Restricted Three Body Problem in non-dimensional frame

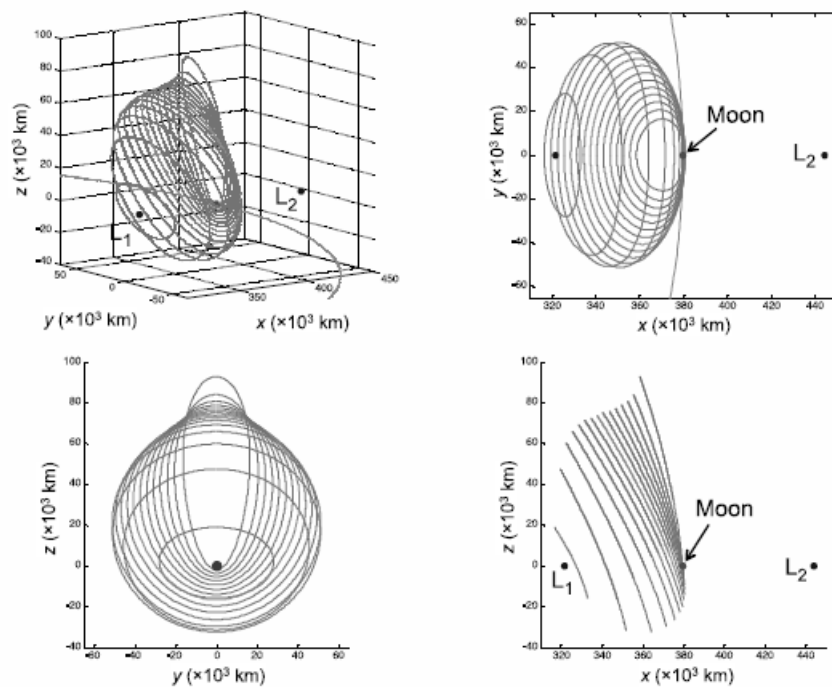


Figure 2-Several example orbits from the family of halo orbits about the Earth-Moon L1 point.

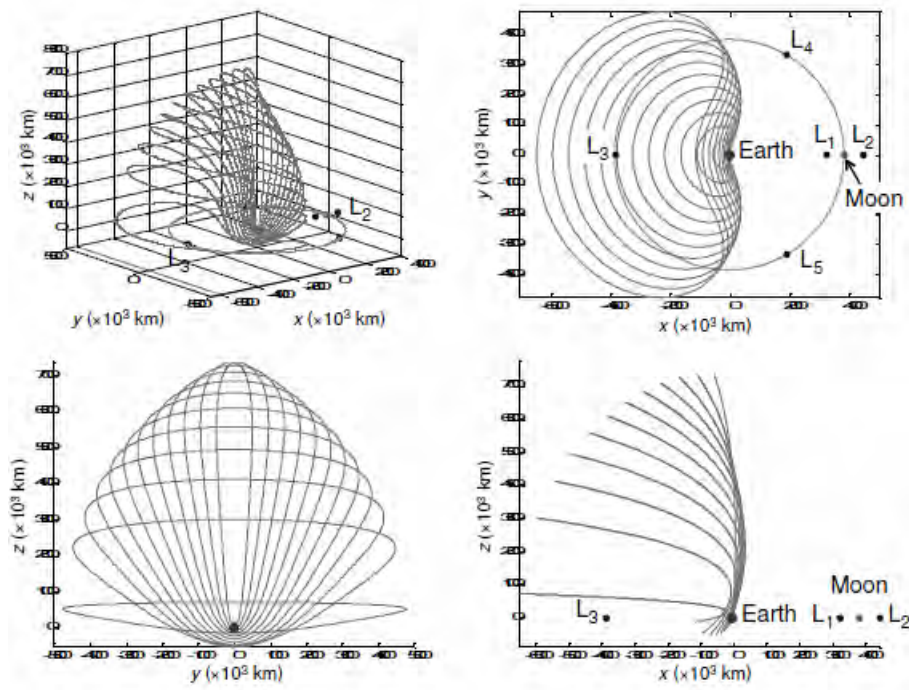


Figure 3-Several example orbits from the family of halo orbits about the Earth-Moon L_3 point.

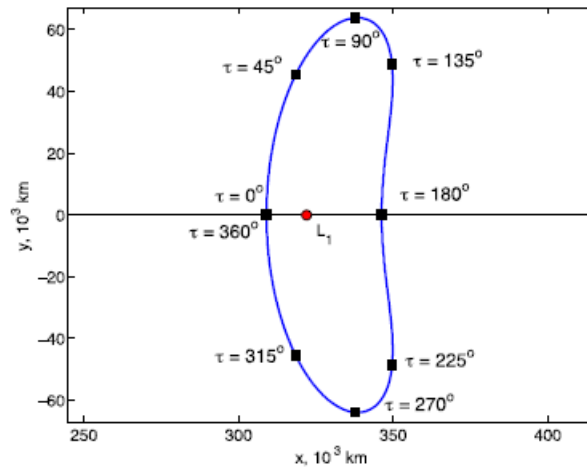


Figure 4-Values of τ around a periodic orbit.

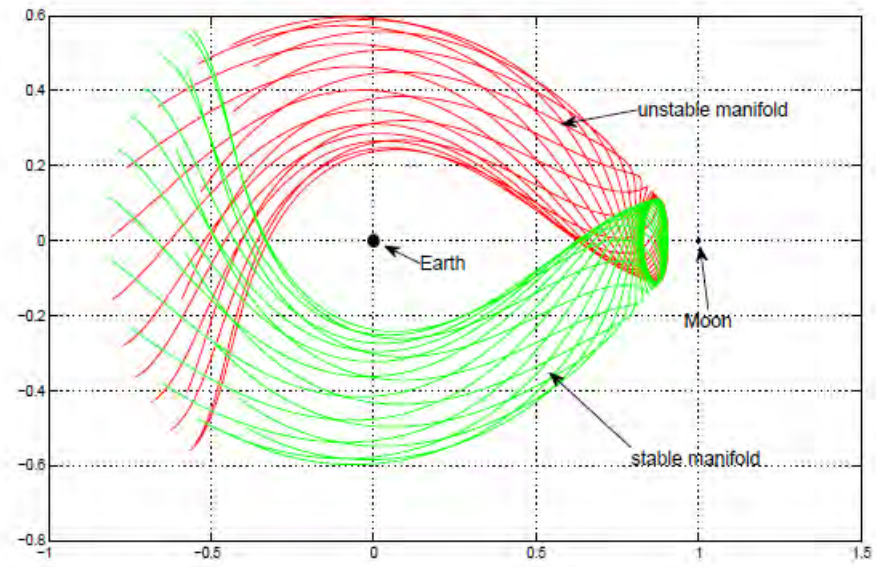


Figure 5-Stable (green) and unstable (red) exterior manifolds of an L1 halo orbit.

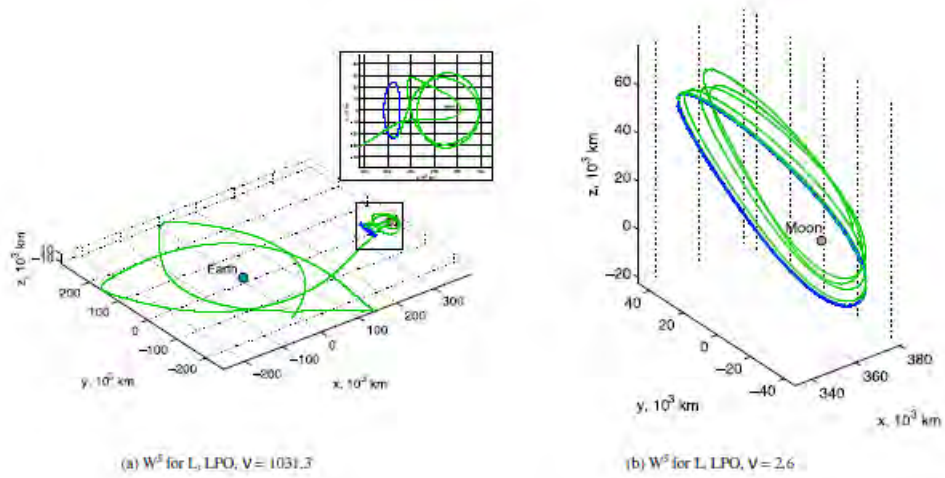


Figure 6-Stable manifold trajectories of two L1 LPOs with significantly different stability coefficients

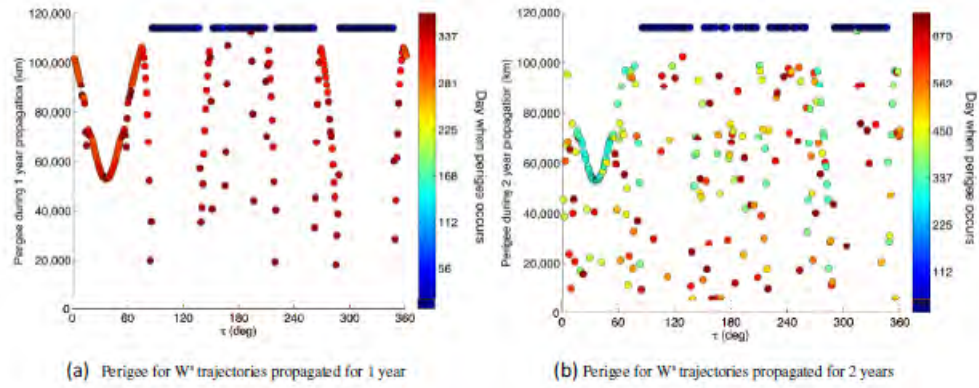


Figure 7-The perigees of WS trajectories of an L3 halo orbit with $C=2.42$ propagated for one year (left) and two years (right). The color of the marker indicates the day on which perigee occurs.

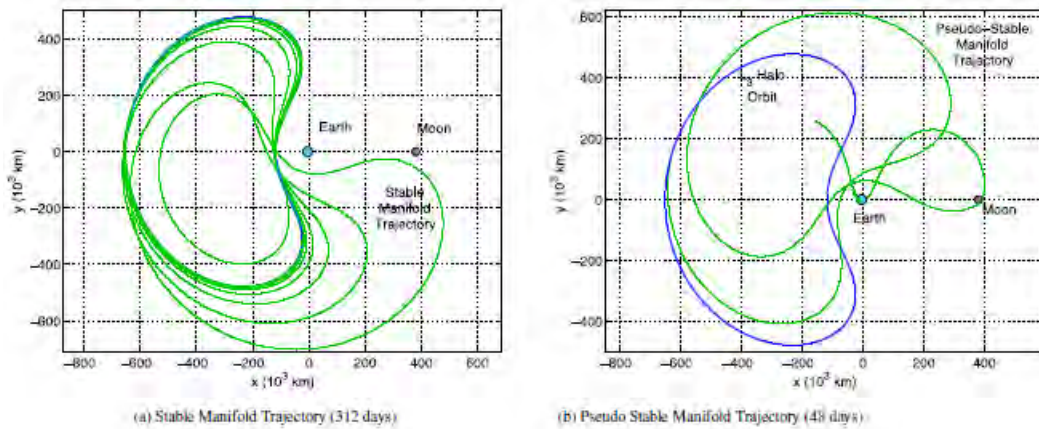


Figure 8-Planar views of the stable (left) and pseudo-stable (right) manifold trajectories which depart from the same location on the nominal L3 halo orbit.

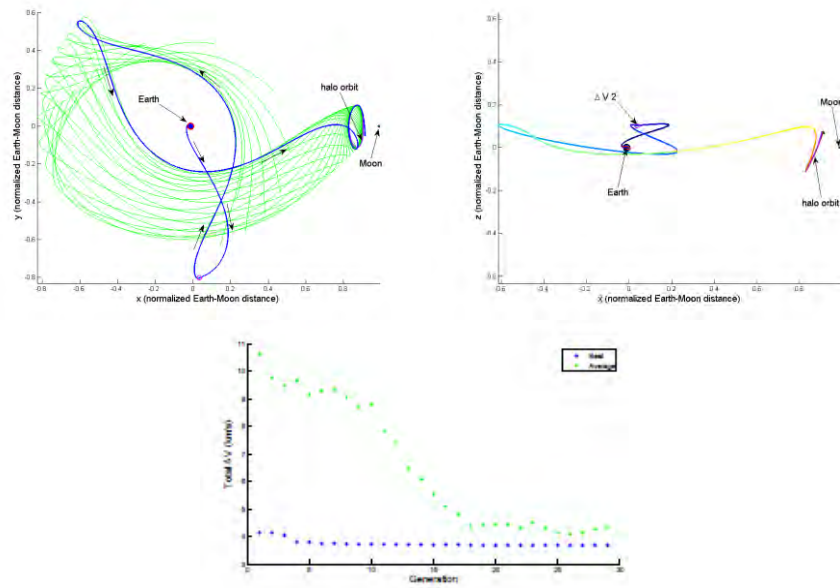


Figure 9-Optimal two-impulse transfer from LEO to a southern L1 halo orbit with $C=3.10$. Delta- v_2 is indicated by the pink circle. The genetic algorithm scatter plot is shown converging to the optimal solution

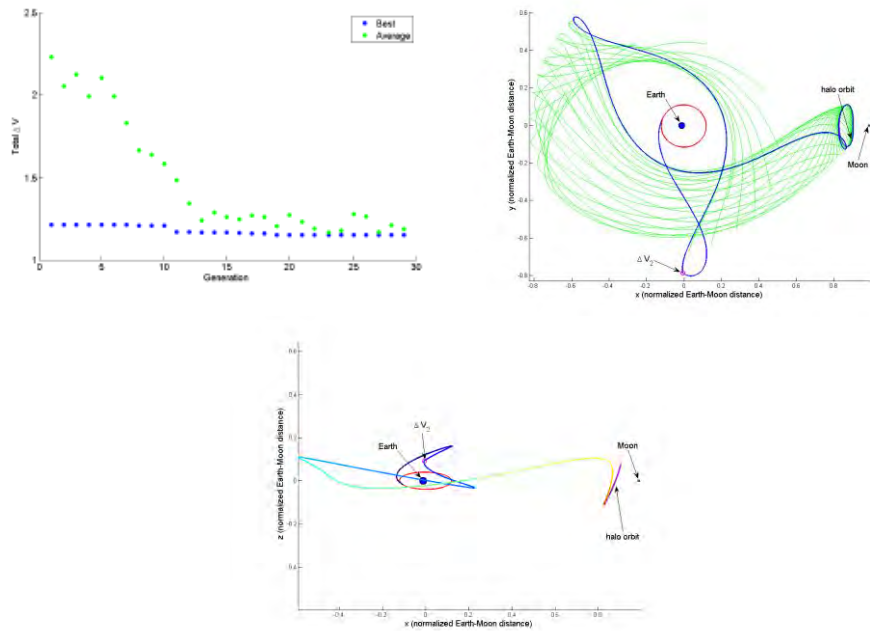


Figure 10-Optimal two-impulse transfer from GEO to a southern L1 halo orbit with $C=3.10$. Delta- v_2 is indicated by the pink circle. The genetic algorithm scatter plot is shown converging to the optimal solution.

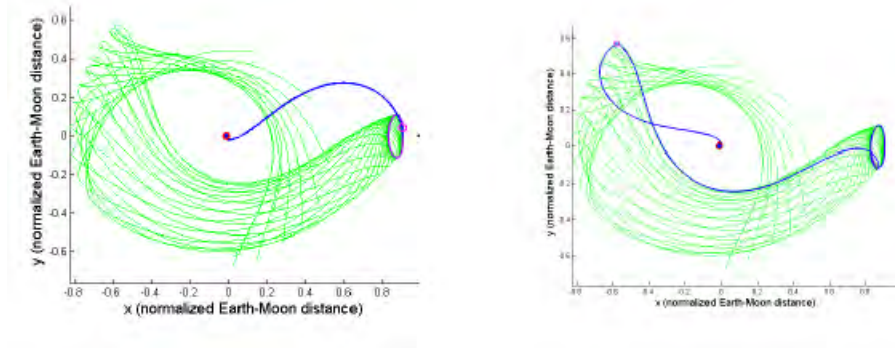


Figure 11-Direct and an alternative locally optimal transfer from LEO to a southern L1 halo orbit with $C=3.10$. Delta- v_2 is indicated by the pink circle.

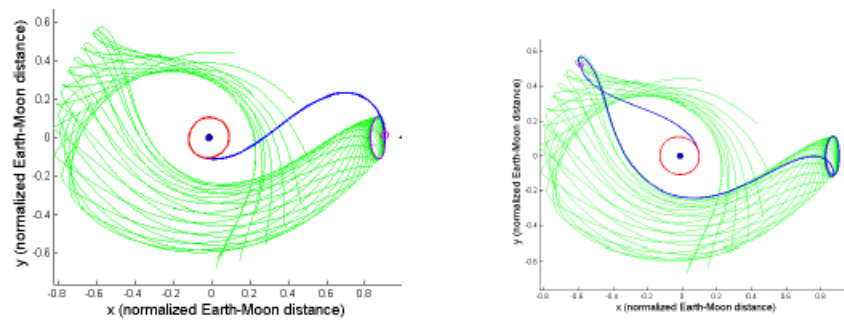


Figure 12-Direct and an alternative locally optimal transfer from GEO to a southern L1 halo orbit with $C=3.10$. Delta- v_2 is indicated by the pink circle.

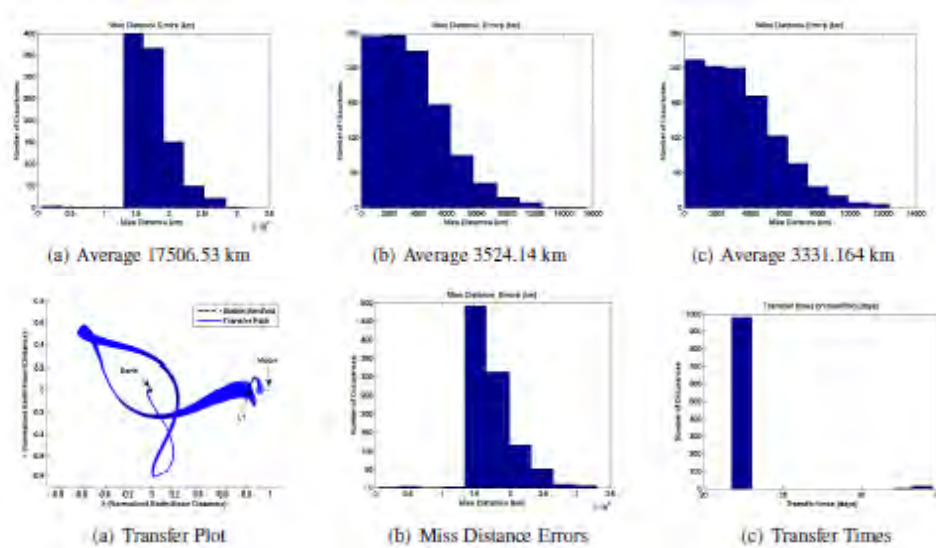


Figure 13-Effects of thrust magnitude and direction dispersions at manifold injection on miss distance and transfer times without guidance for LEO transfers. Miss distance dispersions are for thrust errors in magnitude, in-plane direction, out-of-plane direction

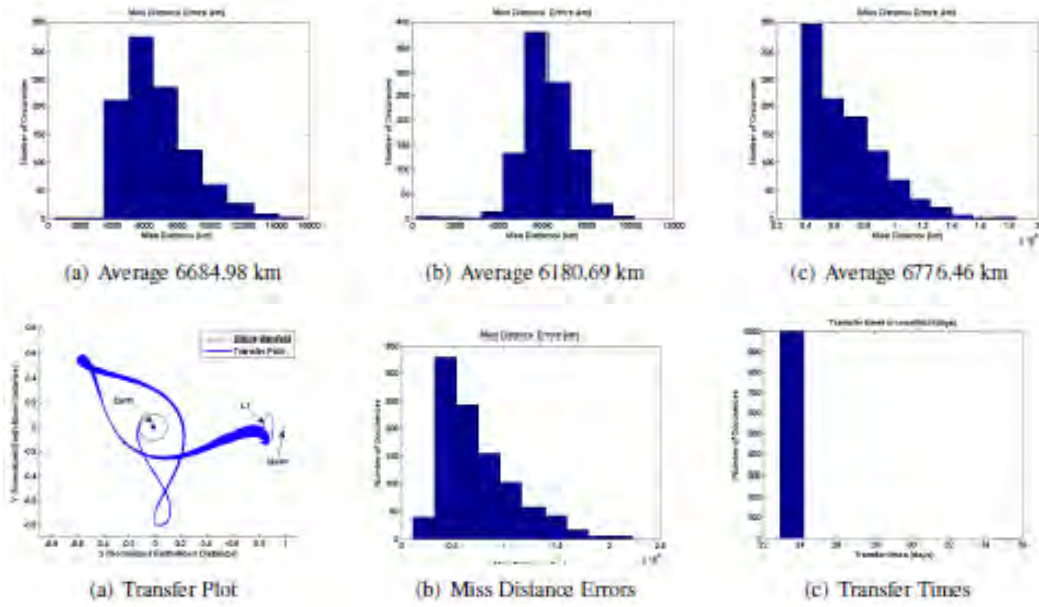


Figure 14-Effects of thrust magnitude and direction dispersions at manifold injection on miss distance and transfer times without guidance for GEO transfers. Miss distance dispersions are for thrust errors in magnitude, in-plane direction, out-of-plane direction

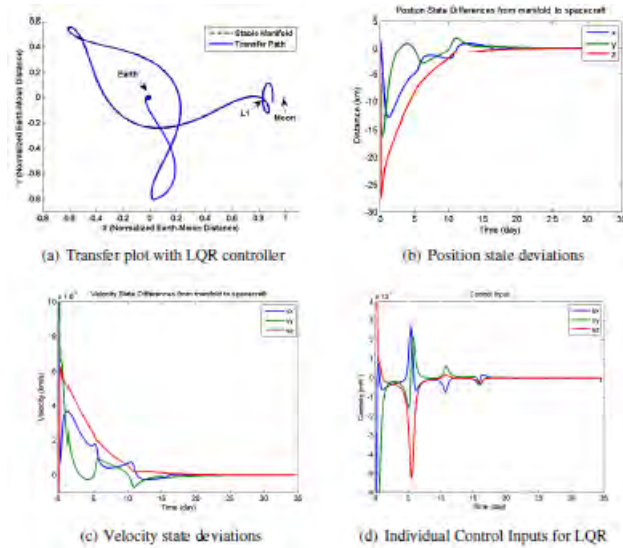


Figure 15- LQR-based guidance with manifold injection errors for L1 halo orbit transfer from LEO.

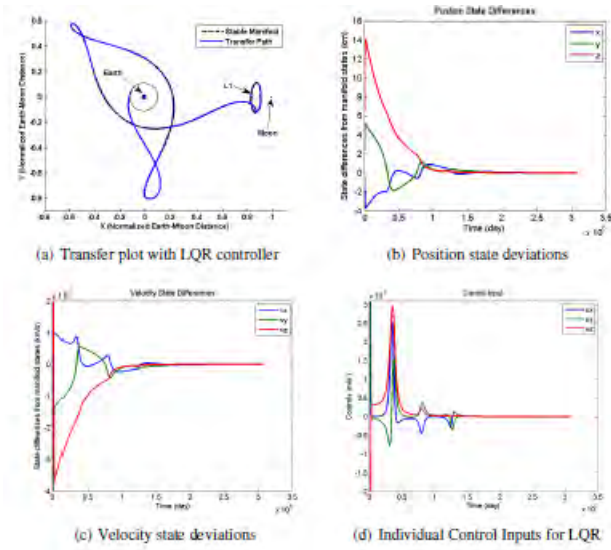


Figure 16-LQR-based guidance with manifold injection errors for L1 halo orbit transfer from GEO.

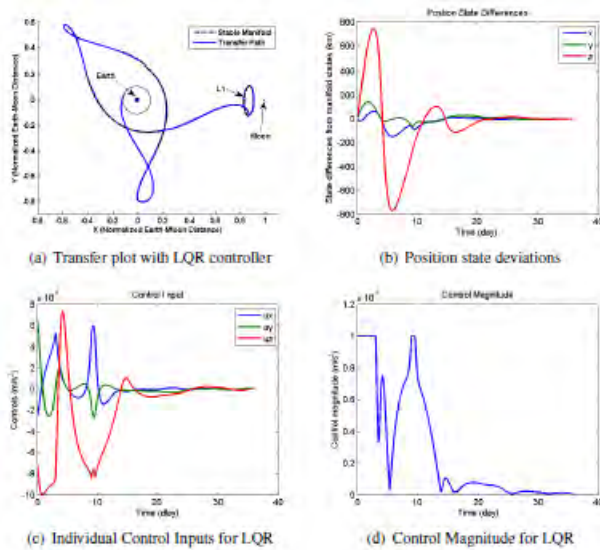


Figure 17-LQR-based limited thrust guidance ($T_m = 0.01 \text{ mm/s}^2$) with manifold injection errors for L1 halo orbit transfer from GEO.

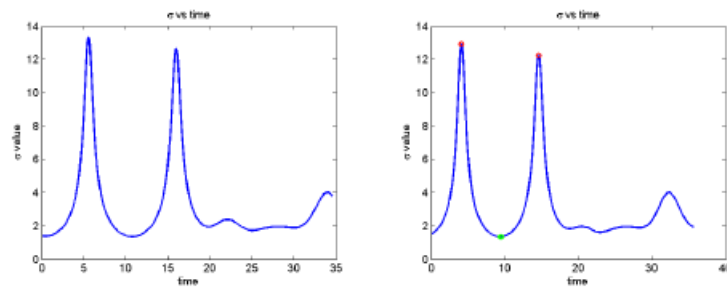


Figure 18-Liapunov exponents for the L1 halo orbit stable manifold associated with the optimal transfers from LEO and GEO in Figs. 9-10.

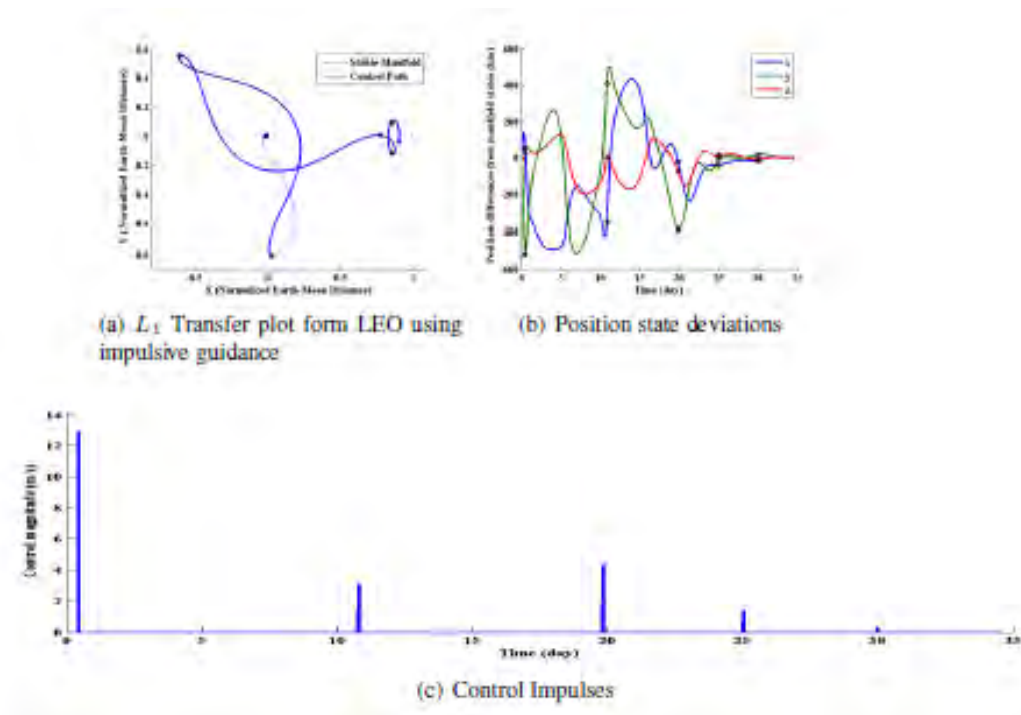


Figure 19-Impulsive guidance with manifold injection and TCM thrust errors using LEO departure.

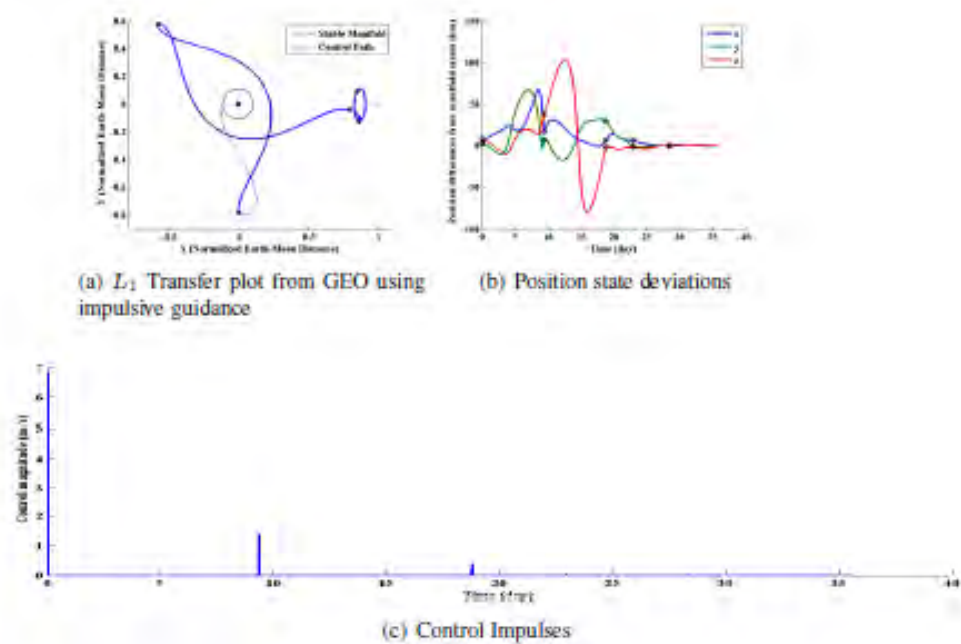


Figure 20-Impulsive guidance with manifold injection and TCM thrust errors using GEO departure.

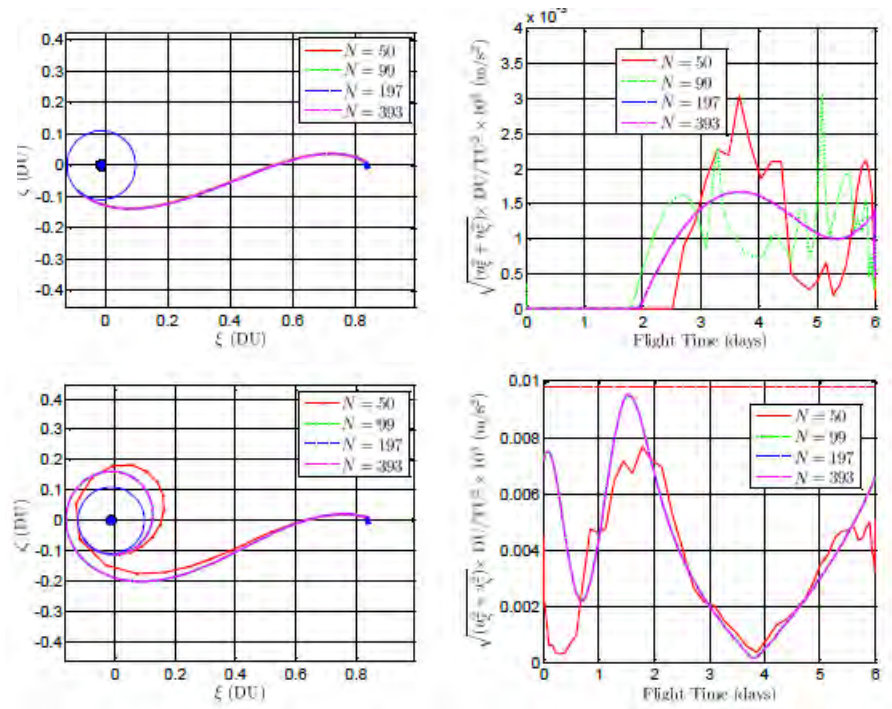


Figure 21-Direct and spiral departure transfer trajectories from GEO to a L1 Liapunov orbit with corresponding continuous thrust magnitudes using mixed impulsive and continuous thrust and quadratic performance index in the OCP.

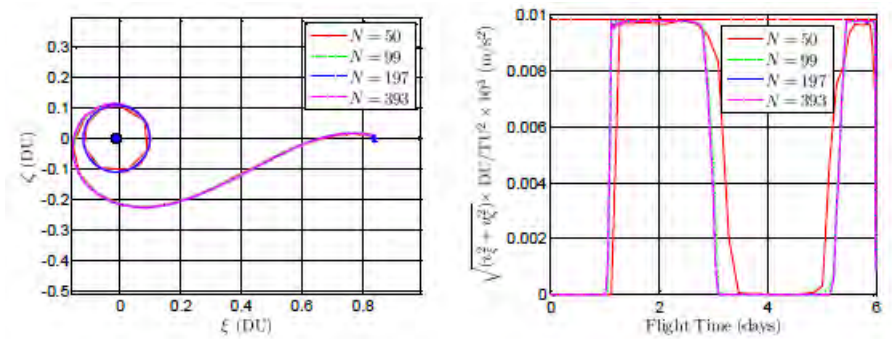


Figure 22-Direct and spiral departure transfer trajectories from GEO to a L1 Liapunov orbit with corresponding continuous thrust magnitudes using mixed impulsive and continuous thrust and minimum fuel performance index in the OCP.

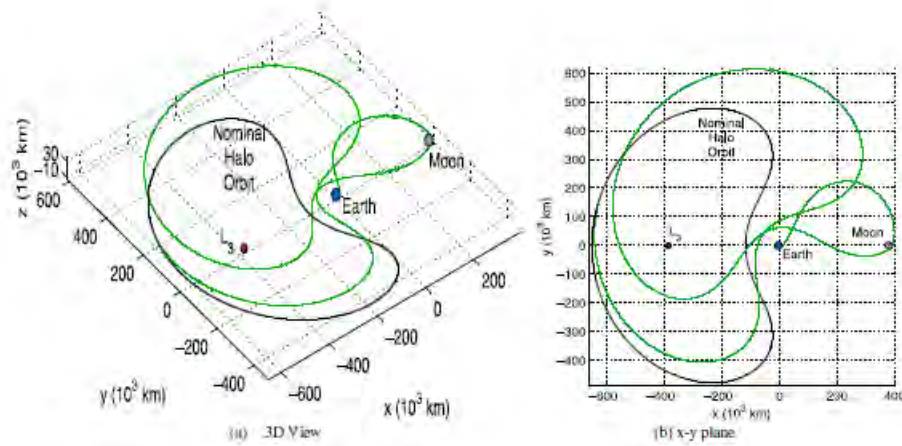


Figure 23-A pseudo-manifold-based transfer trajectory from a 185 km LEO to an L3 halo orbit with $C = 2.40207$.

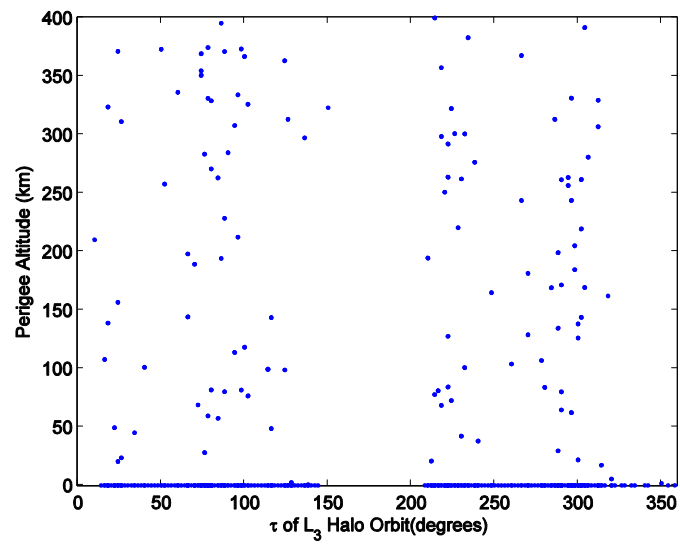


Figure 24-Perigee altitudes (km) for different trajectories with respect to the insertion point into the L3 halo orbit, where $\Delta v_2 = 100$ m/s.

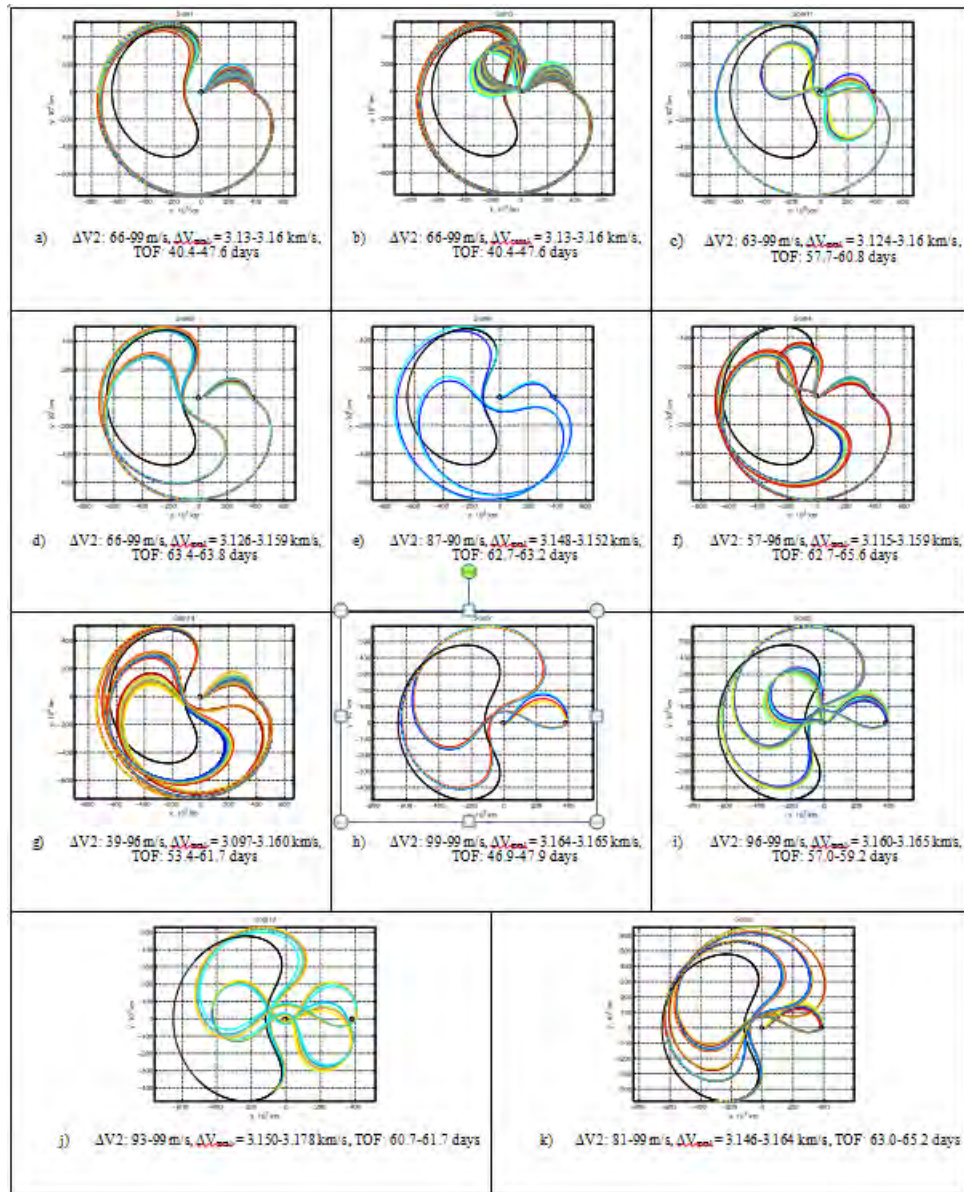


Figure 25-Different families of transfers from a 185 km altitude LEO to the L3 halo orbit.

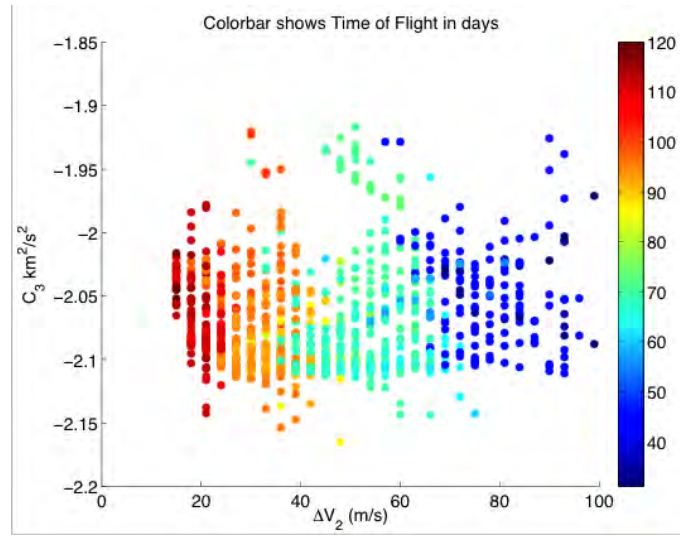


Figure 26- C_3 energy for the departing maneuver with respect to the insertion maneuver into the halo orbit. The color bar shows the flight times in days.

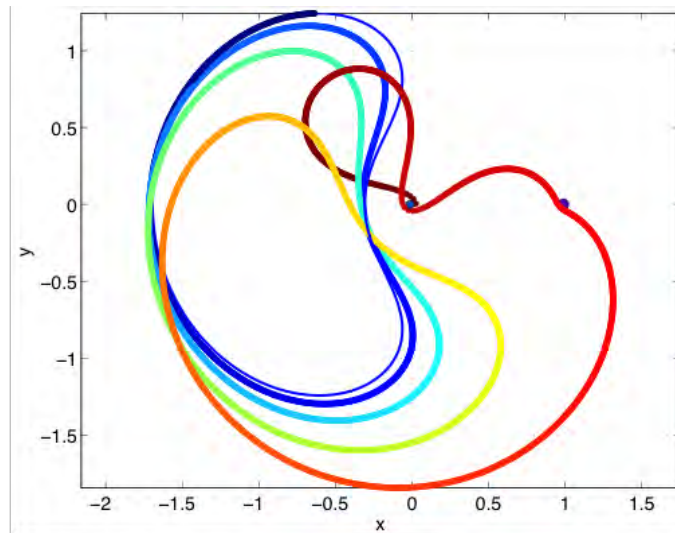


Figure 27-Transfer trajectory to the L3 halo orbit which has the smallest possible insertion maneuver. $C_3 = -2.05 \text{ km}^2/\text{s}^2$, $\Delta V_2 = 0.015 \text{ km/s}$, TOF = 119.6 days.

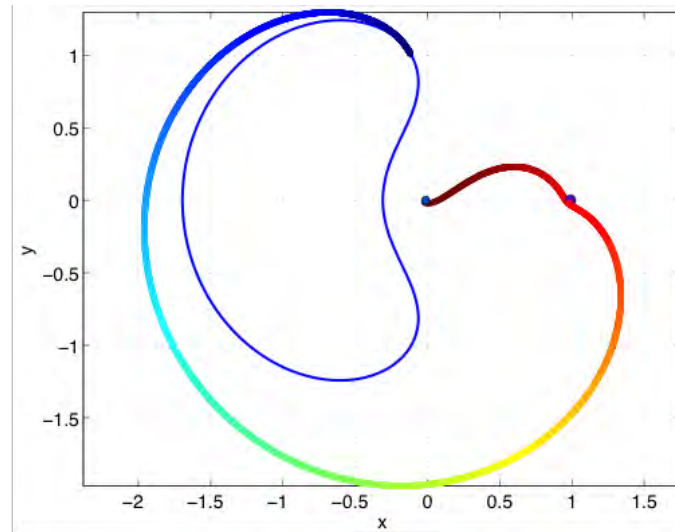


Figure 28-Transfer trajectory to the L3 halo orbit which has the least possible time of flight. $C3=-2.02 \text{ km}^2/\text{s}^2$, $\Delta V2=0.09 \text{ km/s}$, TOF=31 days.

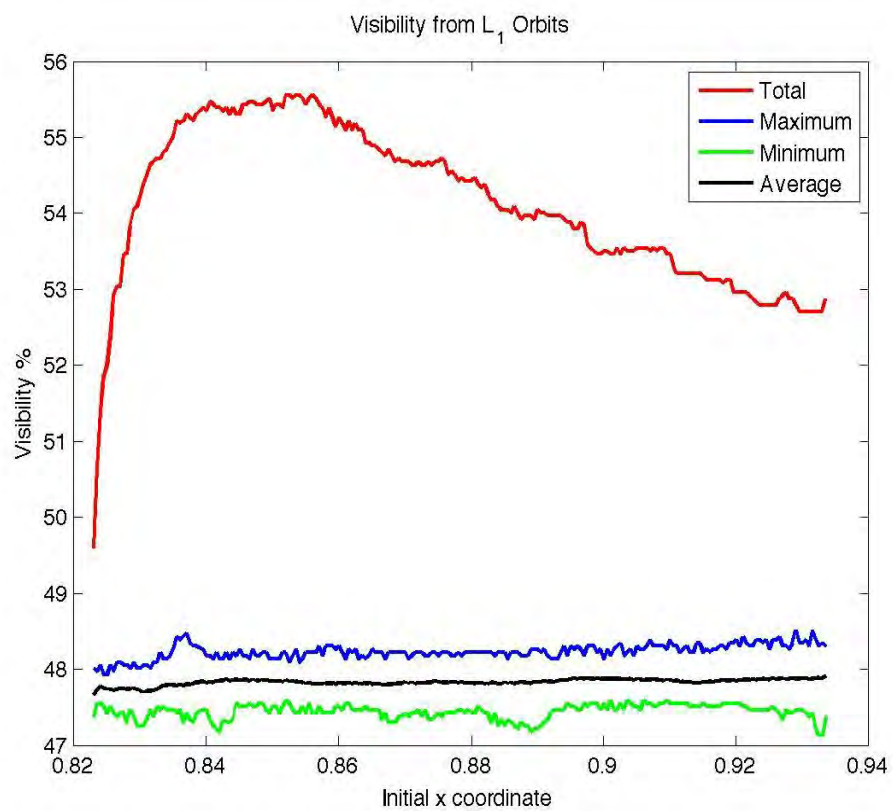


Figure 29-Visibility of Earth surface using a spacecraft on L1 halo orbit

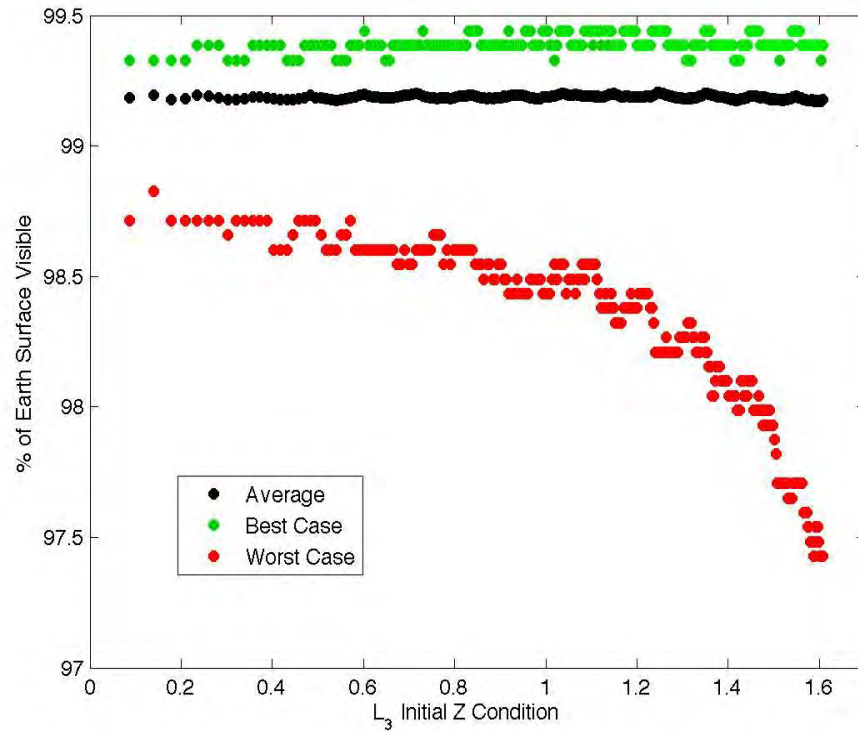


Figure 30-Visibility of geosynchronous orbit using a spacecraft on L1 halo orbit

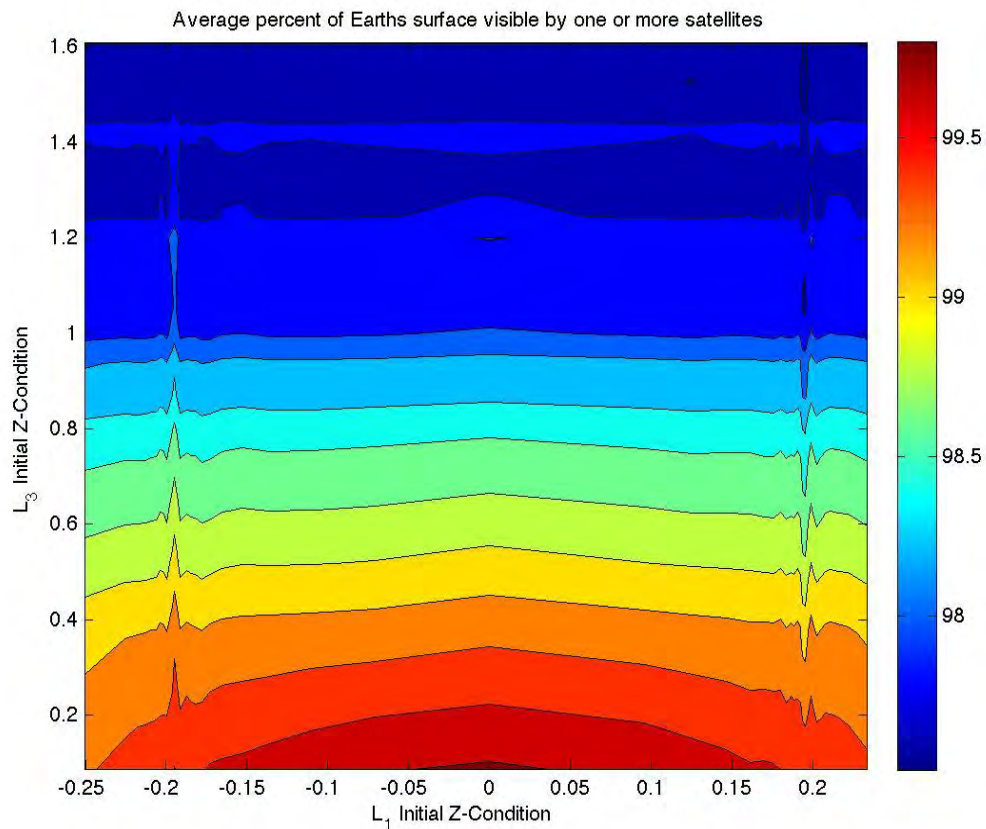


Figure 31-Average percentage of Earth surface visibility by one or more satellites in a constellation of two satellites in L3 halo orbit and one on L1 halo orbit

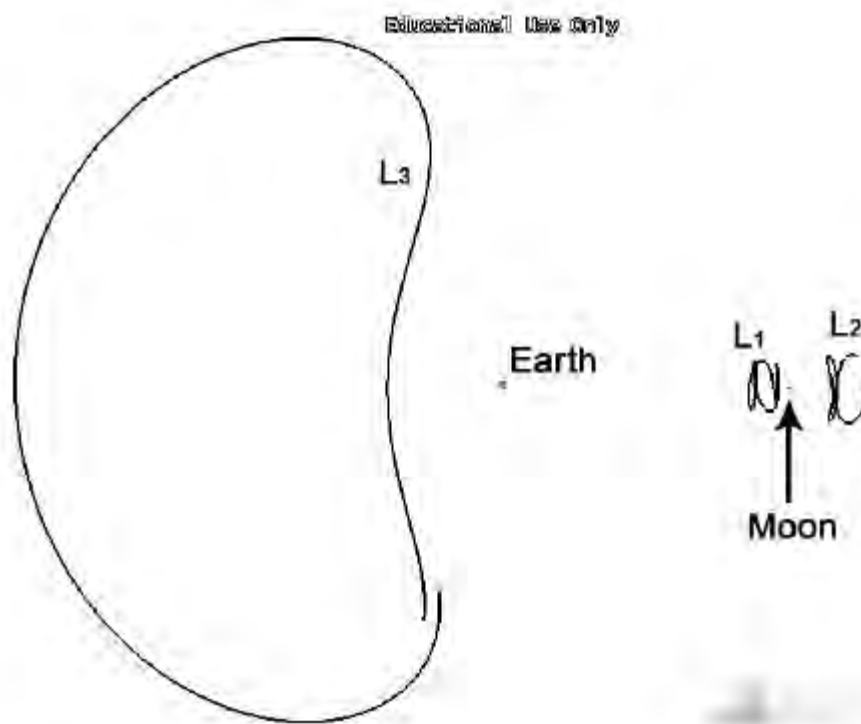


Figure 32-Screenshot of STK showing the L1, L2, and L3 libration point orbits used in the analyses presented here and illustrated in the Earth-Moon rotating coordinate frame

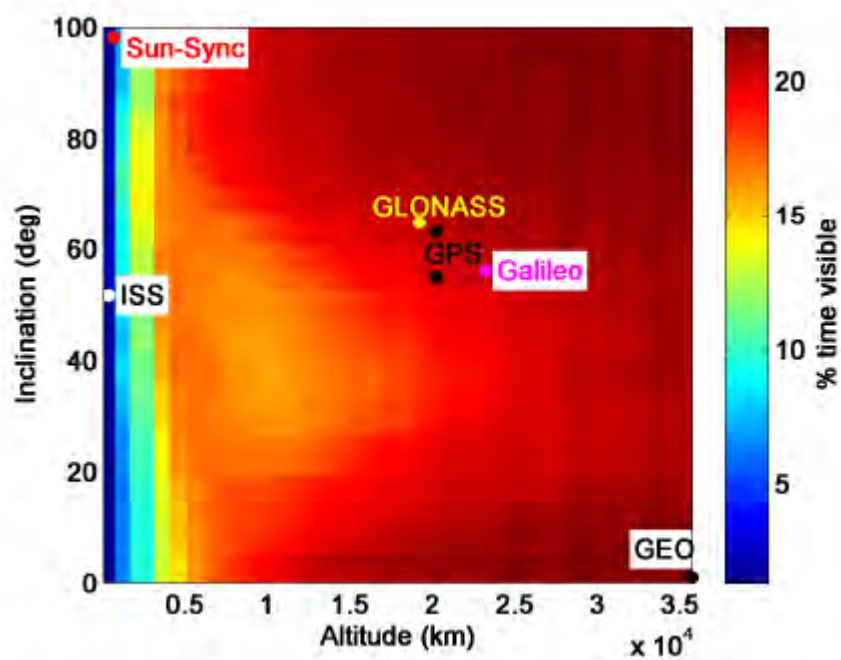


Figure 33-Portion of time where target is visible for various altitudes and inclinations

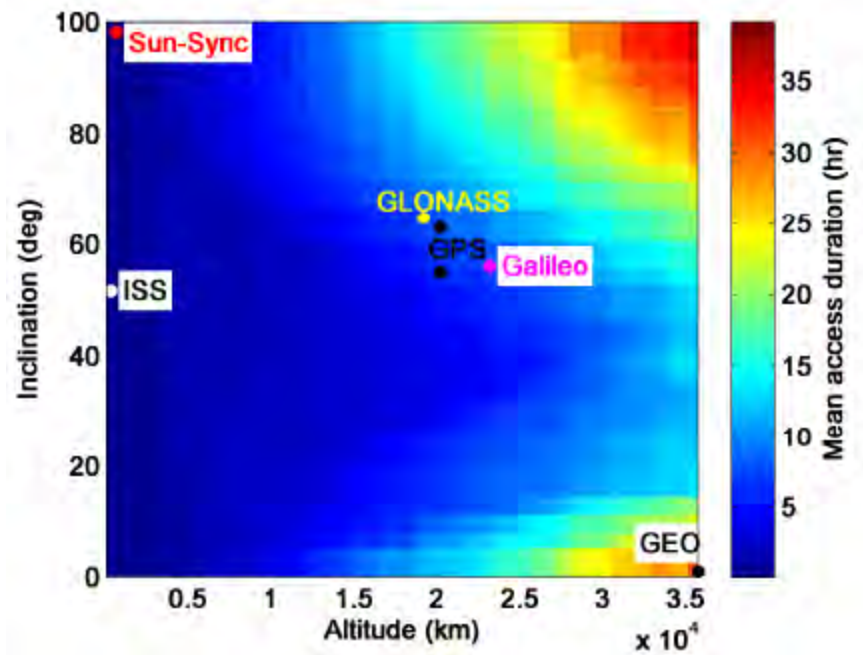


Figure 34-Mean access duration for various altitudes and inclinations.

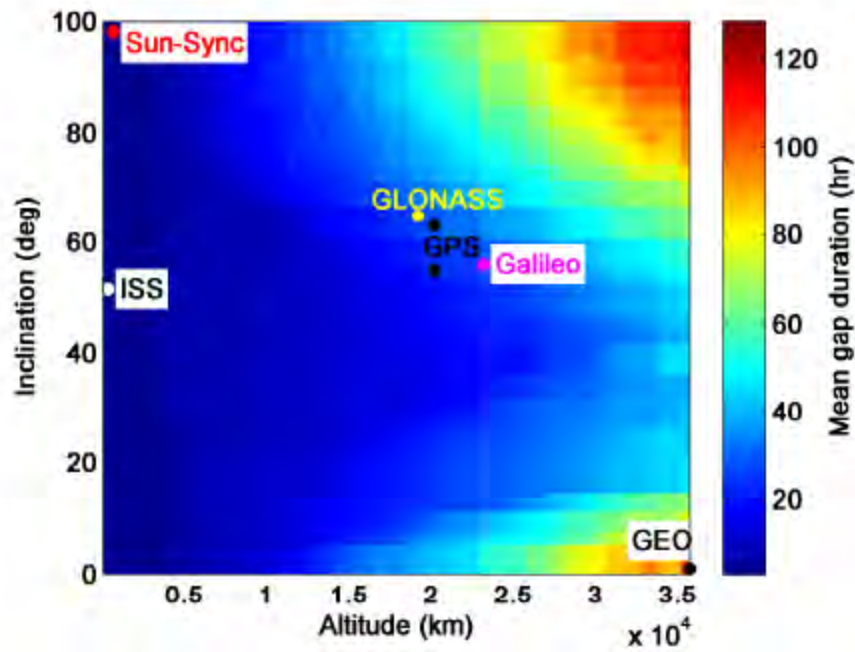


Figure 35-Mean gap duration for various altitudes and inclinations.

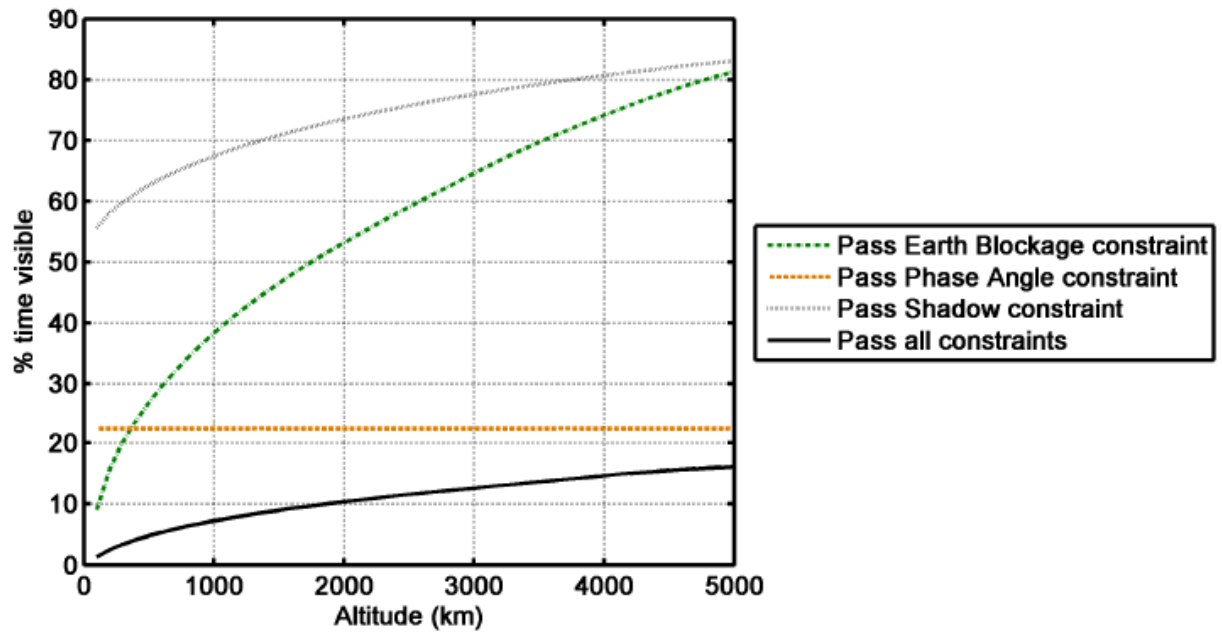


Figure 36-Effect of each constraint on percent time visible for the LEO and MEO regimes.

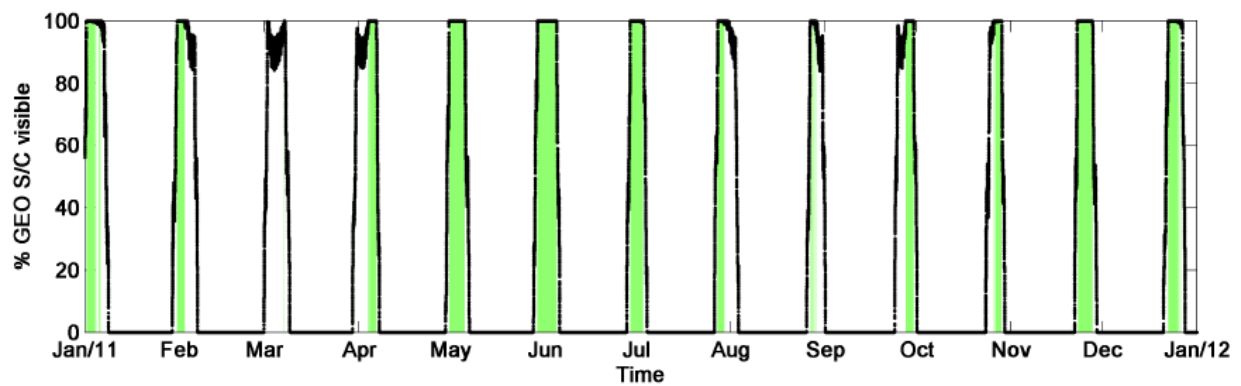


Figure 37-Percentage of GEO spacecraft visible from L1 over time

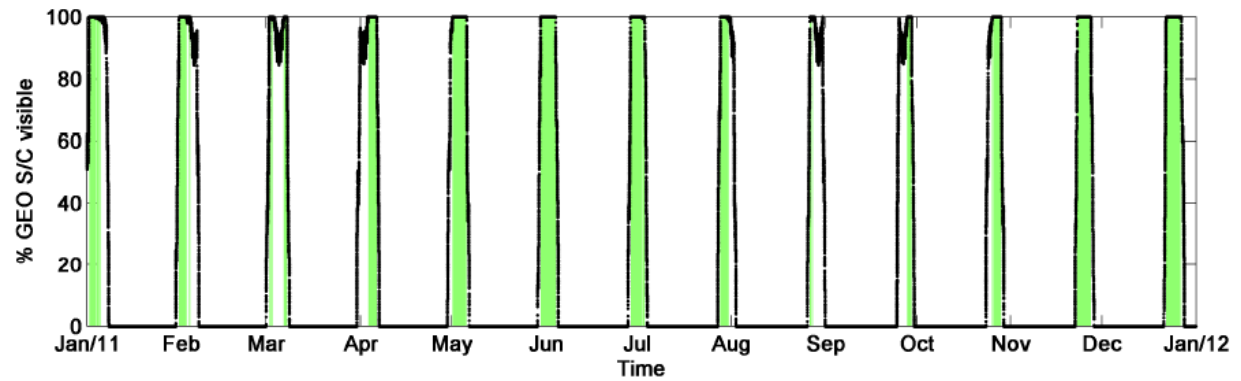


Figure 38-Percentage of GEO spacecraft visible from L2 over time

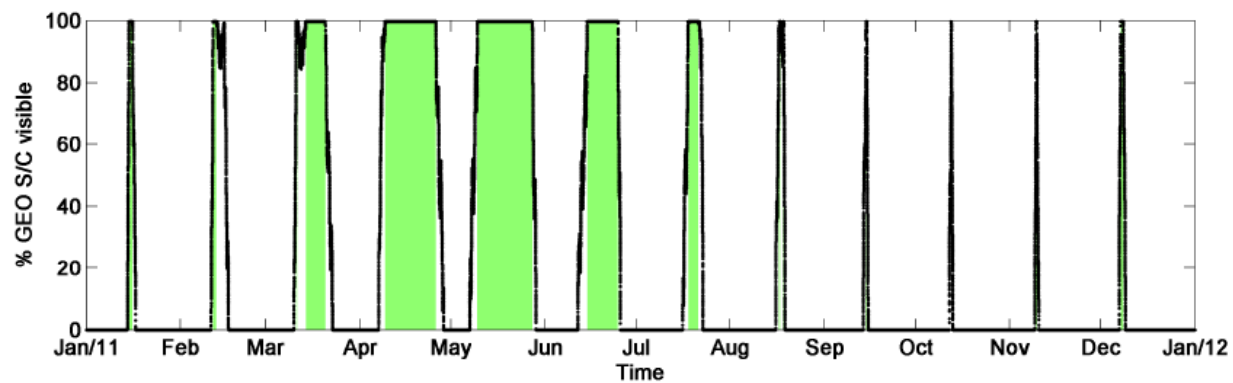


Figure 39-Percentage of GEO spacecraft visible from L3 over time

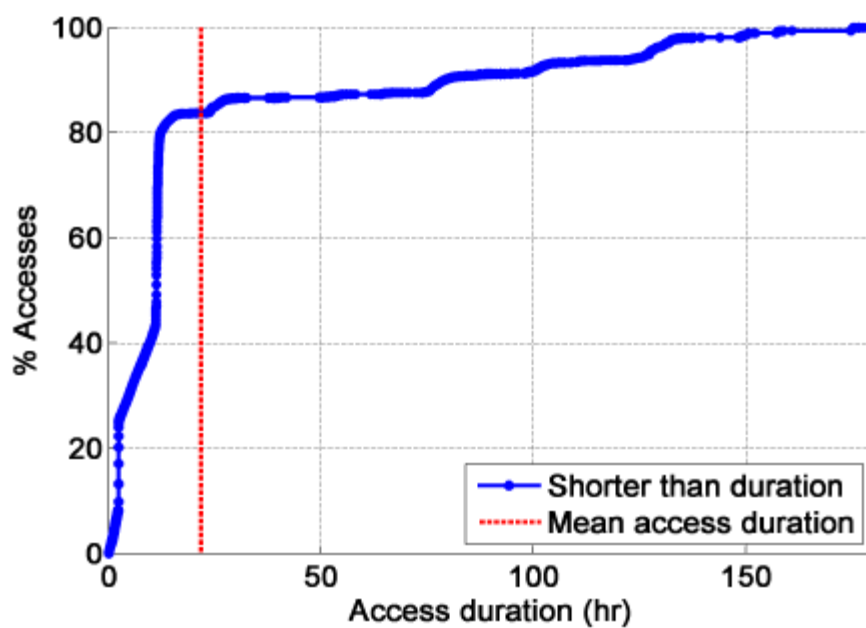


Figure 40-Breakdown of access durations from L1.

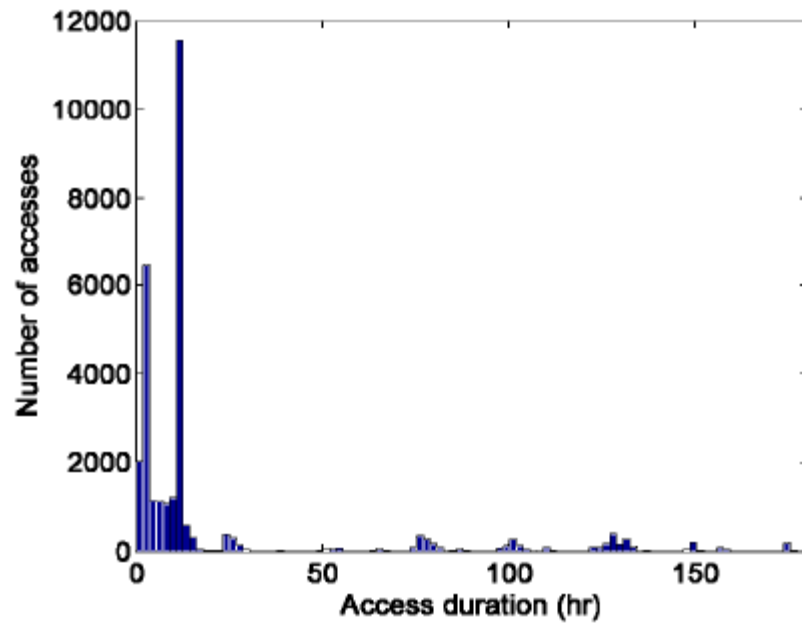


Figure 41-Histogram of access durations from L1

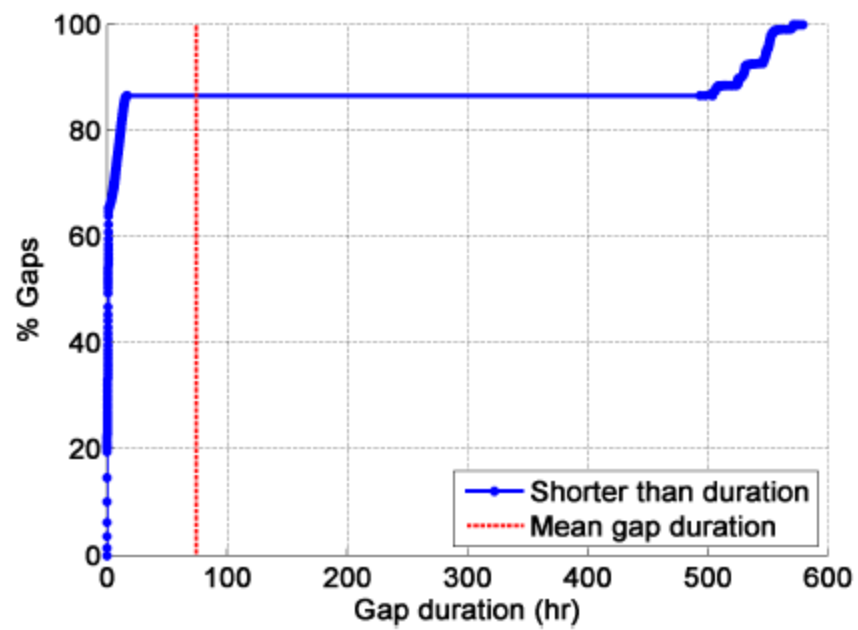


Figure 42-Breakdown of gap durations from L1

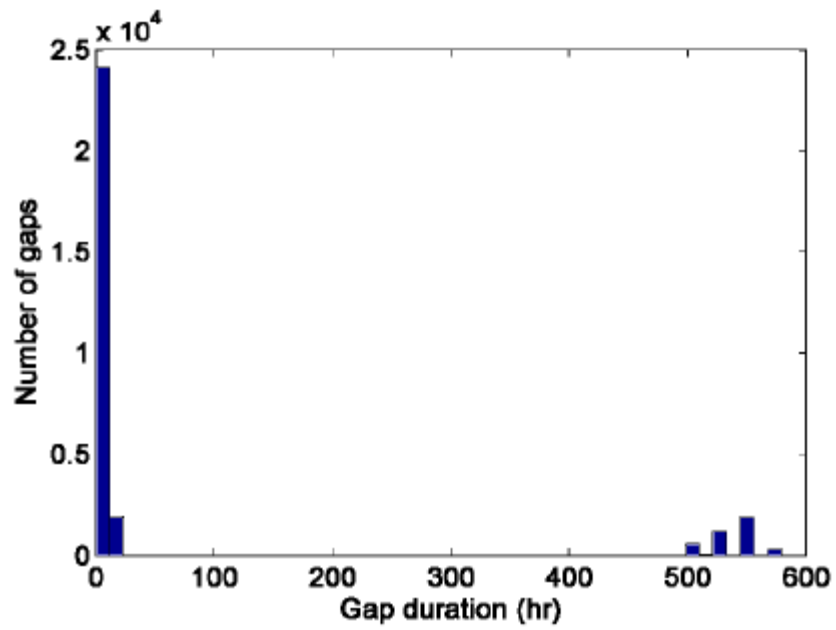


Figure 43-Histogram of gap durations from L1

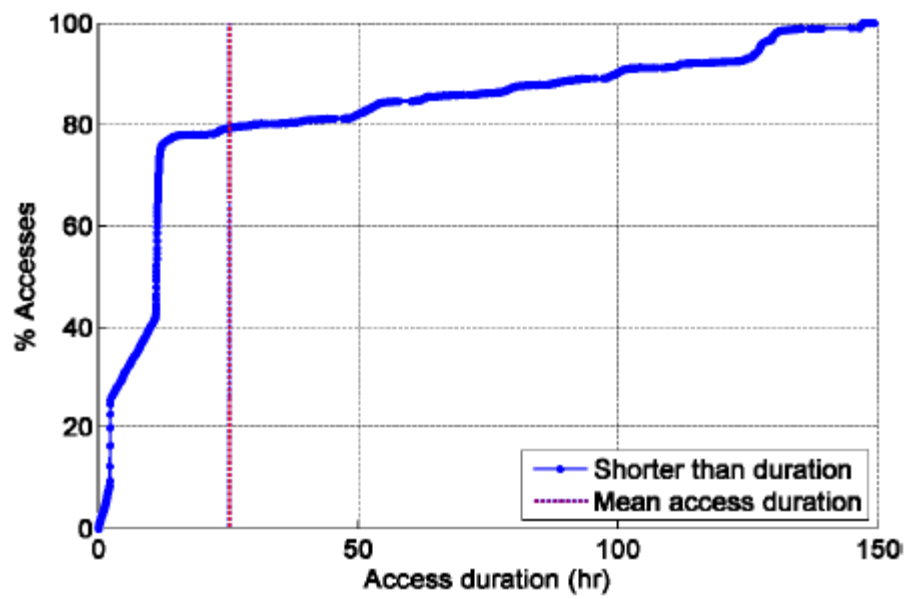


Figure 44-Breakdown of access durations from L2.

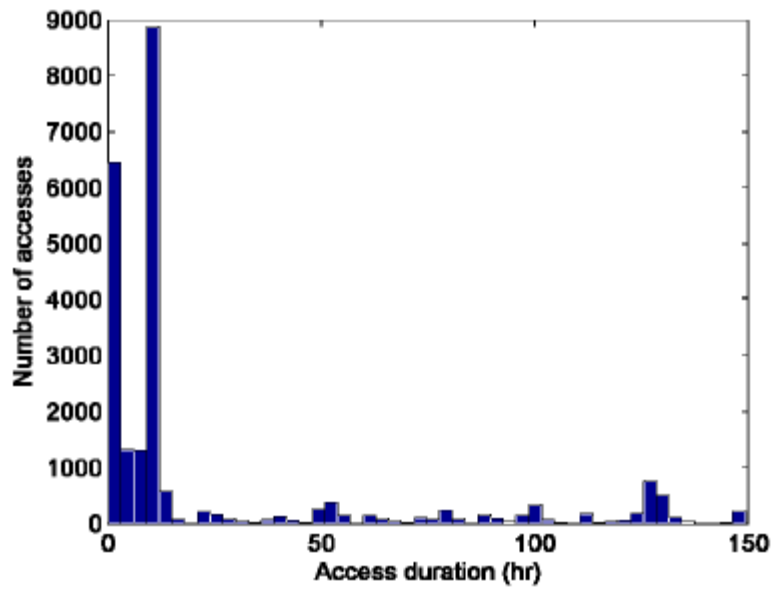


Figure 45-Histogram of access durations from L2

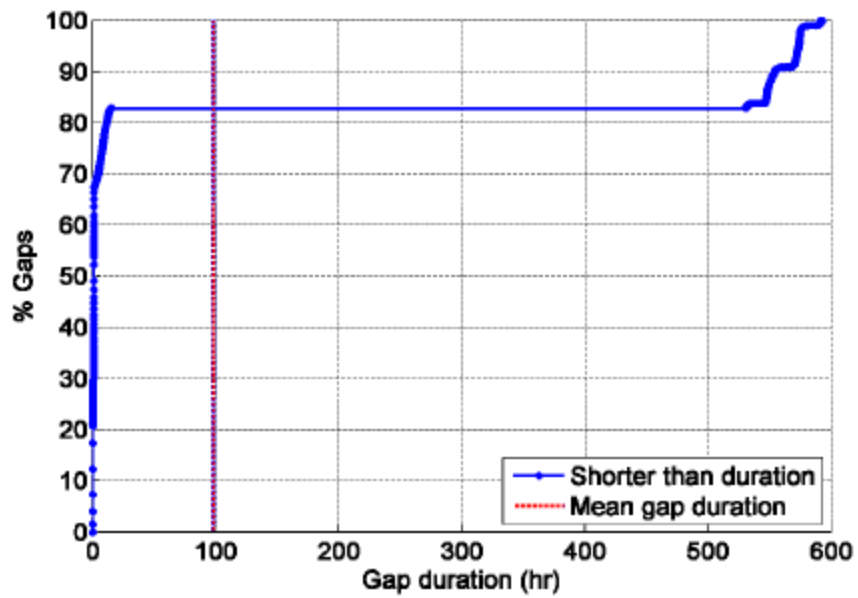


Figure 46- Breakdown of gap durations from L2

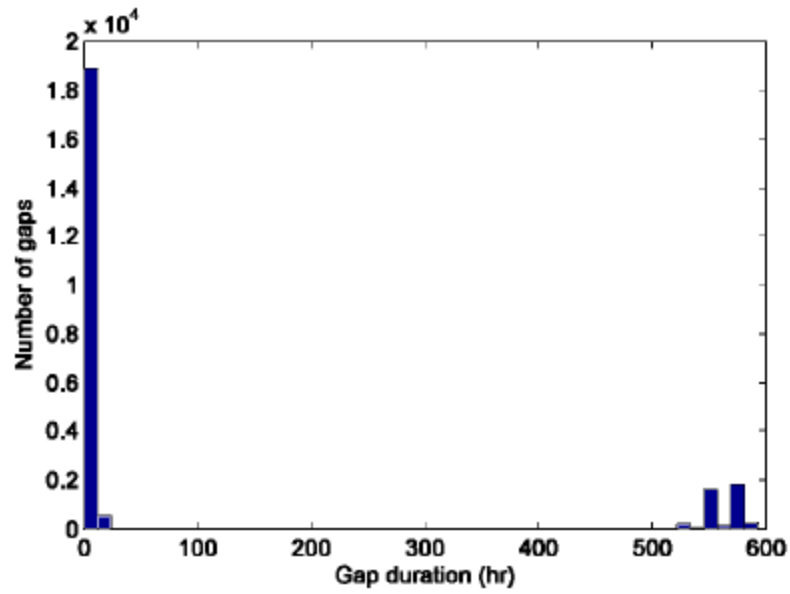


Figure 47-Histogram of gap durations from L2

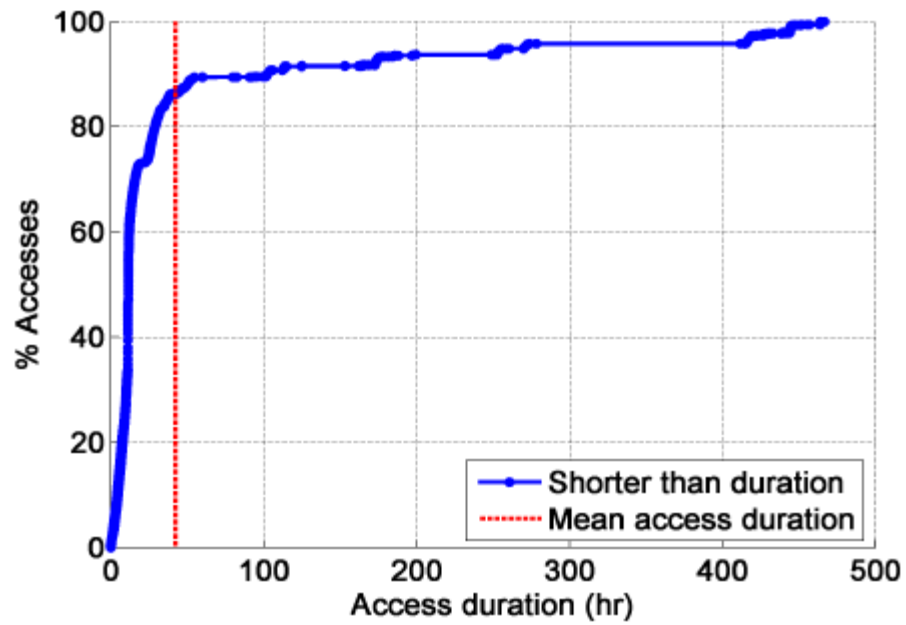


Figure 48-Breakdown of access duration from L3.

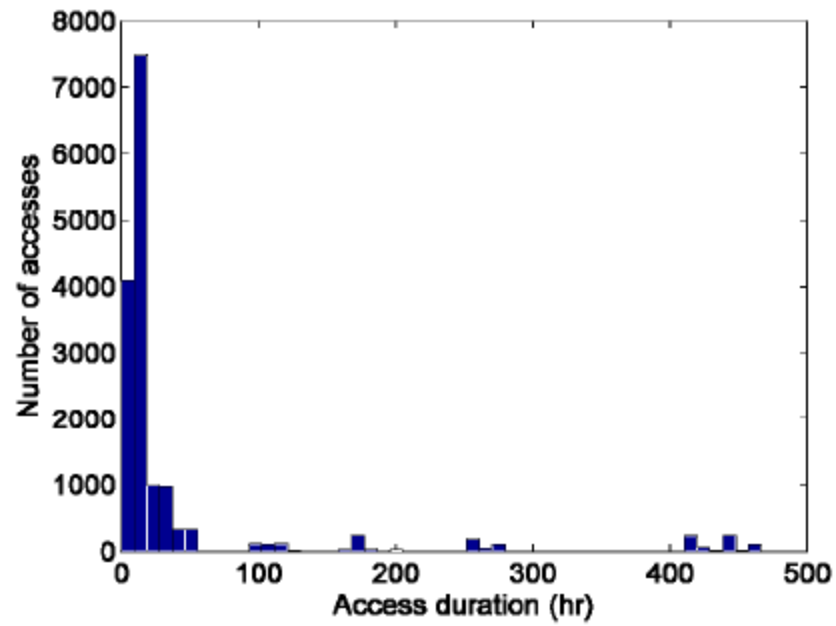


Figure 49-Histogram of access durations from L3

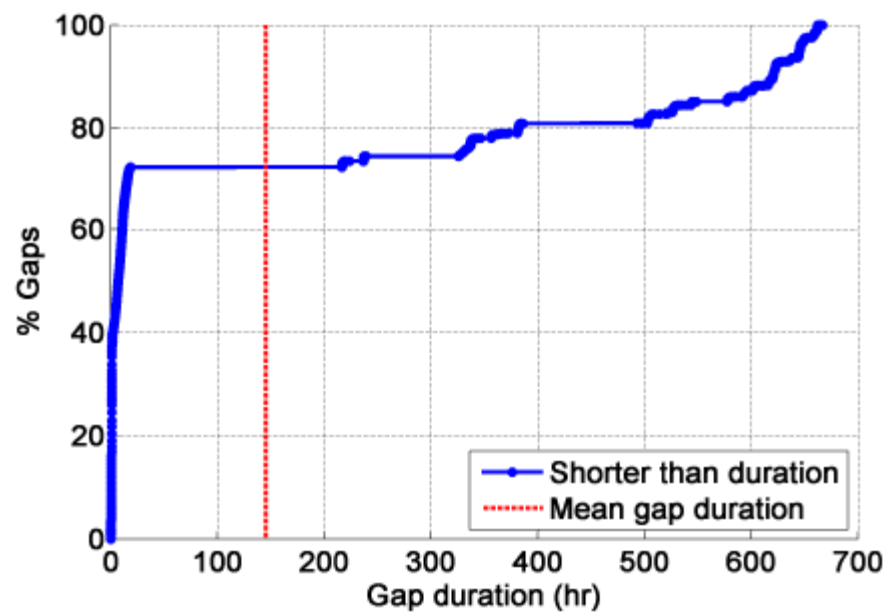


Figure 50-Breakdown of gap duration from L3.

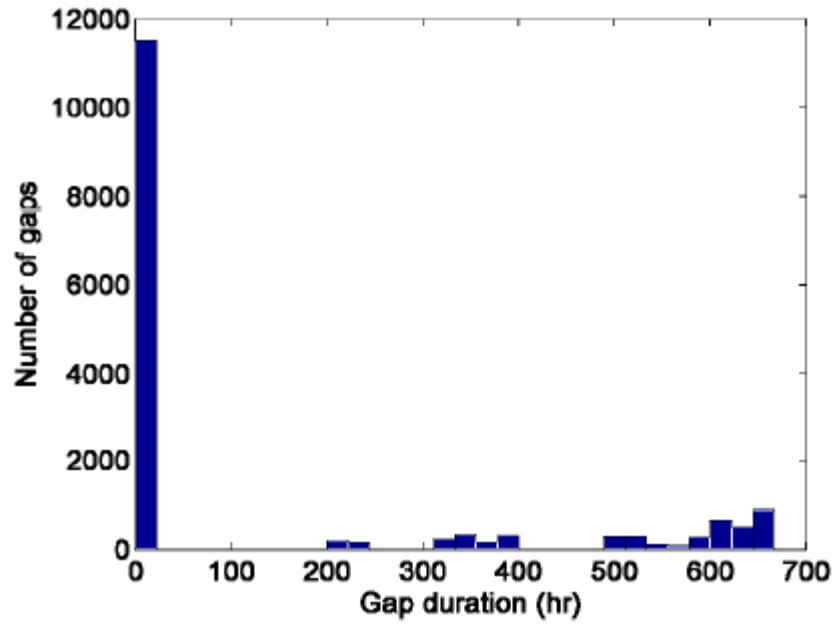


Figure 51-Histogram of gap durations from L3.

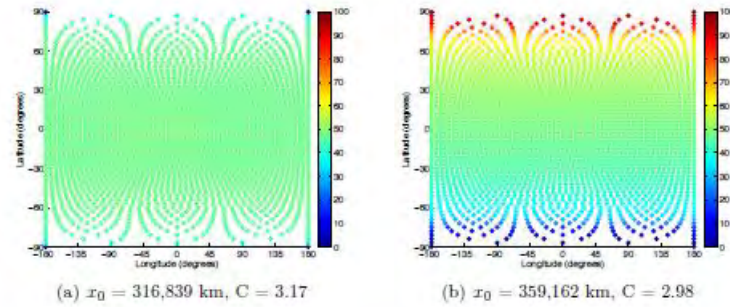


Figure 52-Percent visibility for latitude/longitude points on the Earth surface for selected northern L1 halo orbits assuming Earth's spin axis is identified with z-axis of CR3BP.

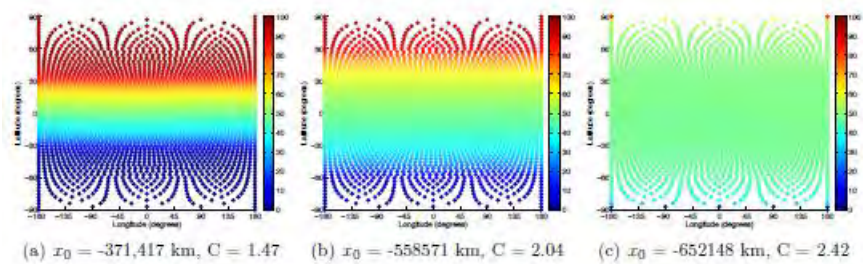


Figure 53-Percent visibility for latitude/longitude points on the Earth surface for selected northern L3 halo orbits assuming Earth's spin axis is identified with z-axis of CR3BP.

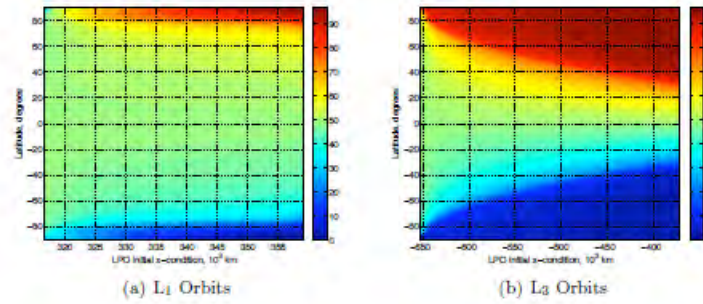


Figure 54-Average Earth visibility by latitude for northern L1 and L3 halo orbits.

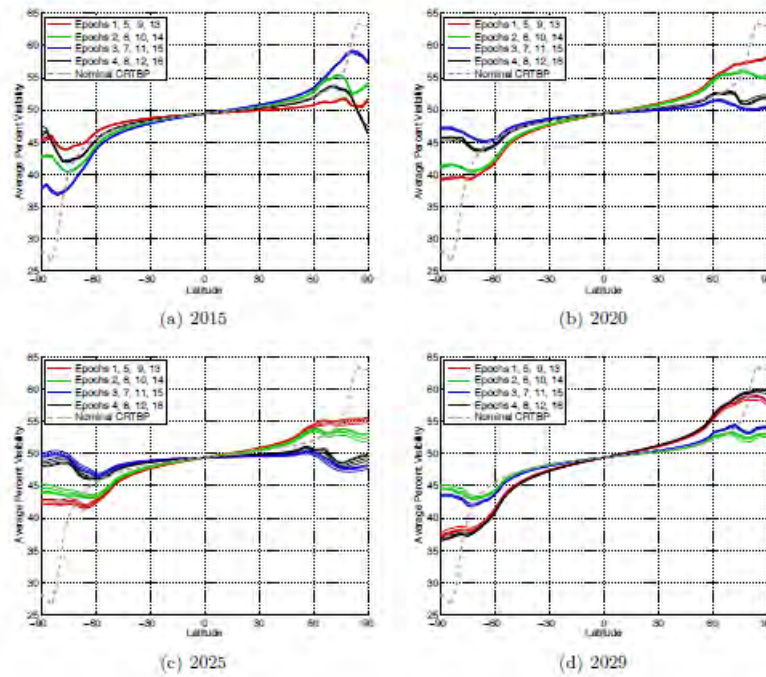


Figure 55-Average visibility by latitude at different ephemeris epochs for an L1 orbiter from STK analysis.

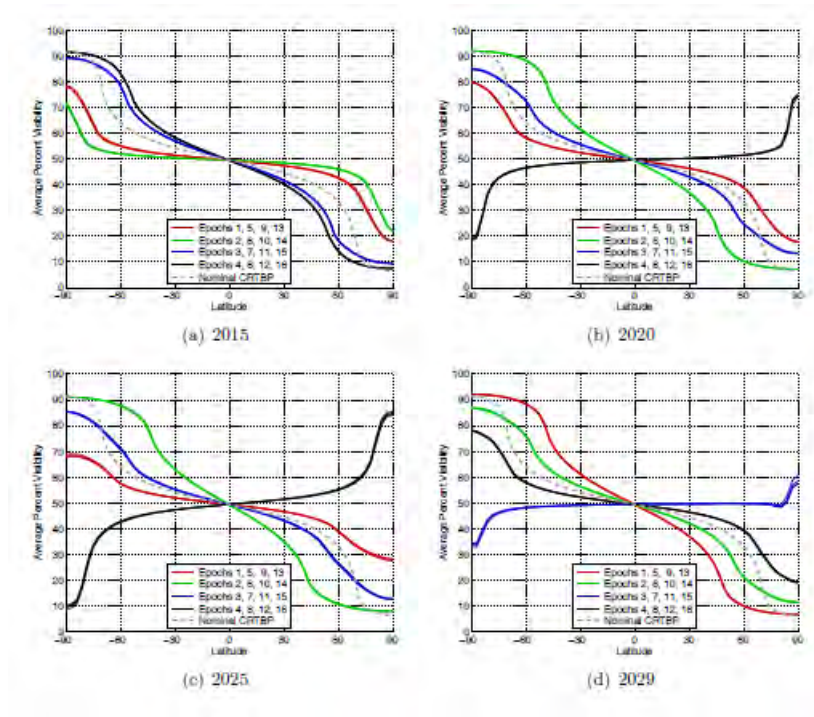


Figure 56-Average visibility by latitude at different ephemeris epochs for an L3 orbiter from STK analysis.

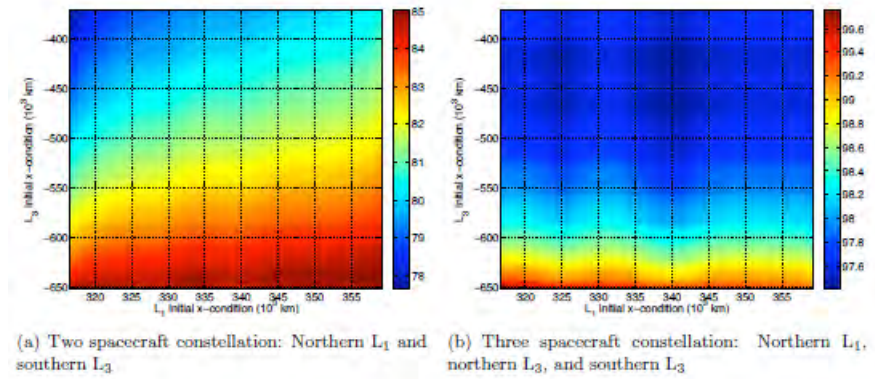


Figure 57-Average percent visibility of the Earth's surface by at least one spacecraft in a constellation of a) two spacecraft and b) three spacecraft in L1 and L3 LPOs.

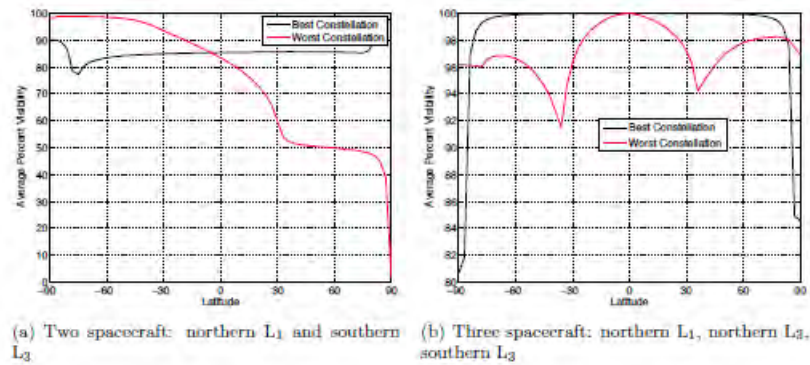


Figure 58-Average percent visibility at each latitude for the constellations that provide the best and worst coverage in a constellation of a) two spacecraft and b) three spacecraft.

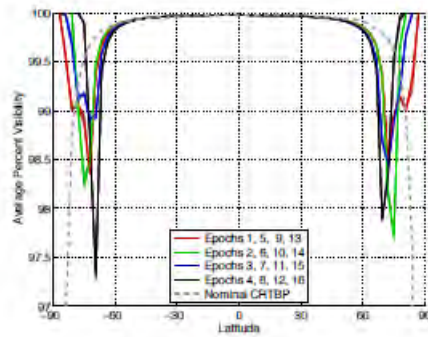


Figure 59-Visibility by latitudes at different ephemeris epochs for a three-spacecraft constellation: comparison of STK analysis (Epochs 1-16) with the nominal CR3BP analysis.